Developed simvastatin chitosan nanoparticles co-crosslinked with tripolyphosphate and chondroitin sulfate for ASGPR-mediated targeted HCC delivery with enhanced oral bioavailability

Tarek M. Faris [a,b,*], Gamaleldin I. Harisa [b,c,d], Fars K. Alanazi [b,c], Ahmed M. Samy [a], Fahd A. Nasr [e]

[a] Department of Pharmaceutics and Industrial Pharmacy, College of Pharmacy, Al-Azhar University, Cairo, Egypt
[b] Kayyali Chair for Pharmaceutical Industry, College of Pharmacy, King Saud University, Riyadh, Saudi Arabia
[c] Department of Pharmaceutics, College of Pharmacy, King Saud University, Riyadh, Saudi Arabia
[d] Department of Biochemistry, College of Pharmacy, Al-Azhar University, Cairo, Egypt
[e] Medicinal Aromatic, and Poisonous Plants Research Center, College of Pharmacy, King Saud University, Saudi Arabia

ABSTRACT

Simvastatin (SV) repurposing has emerged as an alternative approach for the treatment of cancer. In this study, SV chitosan nanoparticles co-crosslinked with tripolyphosphate and chondroitin sulfate (SVCSChSNPs) were developed in order to maximize SV therapeutic efficiency. The hepatic targeting was realized using N-acetylgalactosamine (GalNAc) residues of ChS, which can be identified by the ASGPR receptors specifically expressed in hepatocytes. SV was repurposed as an anticancer agent against hepatocellular carcinoma (HCC). NPs were fabricated by the ionic gelation method, and the formulation variables (CS concentration, CS:ChS ratio, and CS solution pH) were optimized using a three-factor, three-level Box-Behnken design. The optimized NPs were investigated for particle size, size distribution, zeta potential, morphology, *in vitro* cytotoxicity, apoptotic effects against human hepatocellular carcinoma HepG2 cells, and detection of intracellular localization. The NPs were further evaluated for *in vitro* release behavior of SV and pharmacokinetics using Wister albino rats. Transmission electron microscopy (TEM) imaging showed a spherical shape with regular surface NPs of < 100 nm diameter. In vitro cytotoxicity testing showed that the SVCSChSNPs exhibited greater inhibition of proliferation in HepG2 cells and high cellular uptake through ASGPR-mediated endocytosis. The *in vitro* dissolution profile was 2.1-fold greater than that of pure SV suspension. Furthermore, *in vivo* oral pharmacokinetics revealed that the obtained NPs enhanced the bioavailability of SV by up to 2- and 1.6-fold for SV and SVA, respectively, compared to the pure SV suspension. These findings demonstrated that hepatic-targeted CSChSNPs delivering SV could potentially serve as a promising platform for HCC and other liver-related diseases.

© 2020 The Author(s). Published by Elsevier B.V. on behalf of King Saud University. This is an open access article under the CC BY-NC-ND license (http://creativecommons.org/licenses/by-nc-nd/4.0/).

1. Introduction

Drug repurposing has garnered considerable attention in the past years, as it offers disease treatment at an affordable cost by using medicine already administered to patients. Statins lower cholesterol by inhibition of the mevalonate pathway. In the past decade, increasing evidence has shown that statins provide other pleiotropic effects, including anti-inflammatory, anti-oxidant, and anticancer activity (Bradbury et al., 2018; Iannelli et al., 2018; Safwat et al., 2017). In this context, repurposing simvastatin (SV), a statin member, as an anticancer agent for the treatment of hepatocellular carcinoma (HCC) has caught researchers' attention (Alkhatib & Al-Merabi, 2014; Harisa, et al., 2017; B. Relja et al., 2011; Relja et al., 2010). HCC is recognized as a serious global health concern and is ranked the second leading cause of cancer-related deaths (World Health Organization, 2018). Currently, available HCC treatments are limited to conventional chemotherapy, kinase inhibitors, and monoclonal antibodies. However, these remedies are limited by high toxicity, non-selectivity, multidrug

* Corresponding author at: College of Pharmacy, King Saud University, P.O. Box 2457, Riyadh 11451, Saudi Arabia.
E-mail addresses: tarek_faris05@yahoo.com (T.M. Faris), harisa@ksu.edu.sa (G.I. Harisa), afars@ksu.edu.sa (F.K. Alanazi), amsahmed1951@yahoo.com (A.M. Samy), fnasr@ksu.edu.sa (F.A. Nasr).

resistance, and adverse reactions (Wang et al., 2018). To address these limitations, the development of tumor-specific agents should be considered. Statins have been suggested for the treatment of HCC because they do not affect DNA and hence do not cause mutation or secondary tumors (Fatehi Hassanabad, 2019).

SV is administered as a lactone pro-drug and is enzymatically hydrolyzed *in vivo* to an active, hydroxy acid form (Nirogi et al., 2007; Oesterle et al., 2017), as shown in Fig. 1. Nevertheless, SV has low oral bioavailability (<5%), which can be ascribed to its low solubility in the gastrointestinal tract and thus its low intestinal absorption, paired with extensive metabolism by the cytochrome-3A (CYP3A) system, specifically cytochrome-3A4 and cytochrome-3A5 enzymes, in the intestine and liver (Geboers et al., 2016). Thus, large oral doses of SV are used to obtain the desired therapeutic action. However, higher dosages than those prescribed for reduction of hyperlipidemia are required for use of SV as an anticancer agent (i.e., 20–80 mg) (Cho et al., 2008; Karimi et al., 2019; Muscella et al., 2014; Wang et al., 2017), which may cause injuries such as myopathy (Matusewicz et al., 2018). Accordingly, it is important to develop drug carriers that address the limitations described. Statins-nanocarriers could be engineered to target tumor cells and consequently reduce drug amount could be recruited (Safwat et al., 2017).

Multiple approaches have been employed to improve the oral *in vivo* efficacy of SV, such as lipid formulation (Zhang et al., 2010a,b), polymeric nanoparticles (Ahmed et al., 2015), dendrimers (Qi et al., 2015), complexes (Kong et al., 2018), self-emulsifying drug delivery systems (SEDDS) (Patil et al., 2007), lipid-based microparticles (Meola et al., 2020), and solid dispersion (Zhang et al., 2016). However, these formulations have some limitations. In the case of SEDDS, a large number of surfactants can irritate the gastrointestinal tract, whereas high concentrations of cyclodextrin can induce hemolysis. Polymeric nanoparticles (NPs) have received considerable attention because they can enhance oral bioavailability and reduce undesirable actions of SV. The bioavailability of NP can be affected by their physicochemical properties, including particle size, shape, surface charge, surface modification, and hydrophobicity (Harisa & Faris, 2019). The proper adjustment of these variables enhances the intracellular uptake of drug delivery systems. NPs with sizes of < 100 nm can avoid uptake by the RES and thus have a prolonged circulation time (Zhao et al., 2019). This facility allows NP accumulation at the tumor site by passive targeting owing to their endothelial permeation and retention (EPR) effect (Torchilin, 2011).

Among the polymers used for the preparation of the drug nanocarriers is chitosan (CS), which is a cationic polysaccharide comprised of β-(1 → 4)-linked D-glucosamine and N-acetyl-D-glucosamine units. CS is a biocompatible, mucoadhesive,

permeability-enhancing polymer. CS attracts to moieties with a negative charge, such as the tumor microenvironment and cell membrane. These features enable chitosan to deliver drugs to the cancer cell (Faris et al., 2020). CS inhibits cancer cell proliferation and potentiates the action of anticancer drugs (Harisa et al., 2016; Jiang et al., 2019; Kou et al., 2017). CS is cross-linked by various methods, such as the ionotropic gelation method (George et al., 2019). This method is widely used, as it involves mild conditions (Fan et al., 2012). However, ionic gelation has many drawbacks; for instance, poor reproducibility, which limits the generalizability of this technique (Jiang et al., 2018).

Chondroitin sulfate (ChS) is an indigenous mucopolysaccharide that consists of b-1,3-linked N-acetylgalactosamine (GalNAc) and b-1,4-linked d-glucuronic acid (GlcA) residues (Barclay et al., 2019). ChS has a wide range of bioactivities, including tissue regeneration, intracellular signaling, and drug delivery systems. GalNAc residues of ChS have specific binding with the asialoglycoprotein receptors (ASGPRs) on hepatocyte membranes. ASGPRs are overexpressed on the surface of hepatocytes, are less common in non-liver cells, and have a high affinity for moieties such as GalNAc and galactose or polymers containing such residues. These moieties can act as ligands for targeted HCC and increase cellular uptake through ASGPR-mediated endocytosis (D'Souza and Devarajan, 2015; Pranatharthiharan et al., 2017; Turato et al., 2017).

ChS is a polyanion that allows interaction with a cationic polyelectrolyte such as CS to form nanoparticles. In CS-ChS nanoformulations, ChS enables the CS crosslinking and makes a ligand-mediated drug delivery through the interaction between GalNAc and ASGPR. The balance between positive charges and negative charges forms NPs with virus-like surfaces, thus allowing increased mucus penetration (Wu et al., 2018). CS-ChS NPs are spontaneously formed after instant CS and ChS mixing (Sharma et al., 2019). However, the NPs formulated may not be uniformly homogeneous. Therefore, in the present study, the CSNS co-crosslinked with TPP and ChS anions were fabricated to increase their rigidity.

A literature review identified some research studies that investigated CSChSNPs as nanocarriers (Ribeiro et al., 2014; Jardim et al., 2015; Umerska et al., 2017). However, these reports examined CSChSNPs for non-oral administration; ChS was the main polymer in the formulation, and some of the studies used delivery systems with a particle size > 200 nm.

This study hypothesizes that a nanocarrier comprising CS and ChS containing GalNAc residues with a particle size < 100 nm might facilitate the cellular uptake of SV by two mechanisms, EPR and ASGPR-mediated targeting of HCC, when orally administered. To the best of our knowledge, little effort has been made to generate CS-functionalized NPs for HCC-targeted oral delivery.
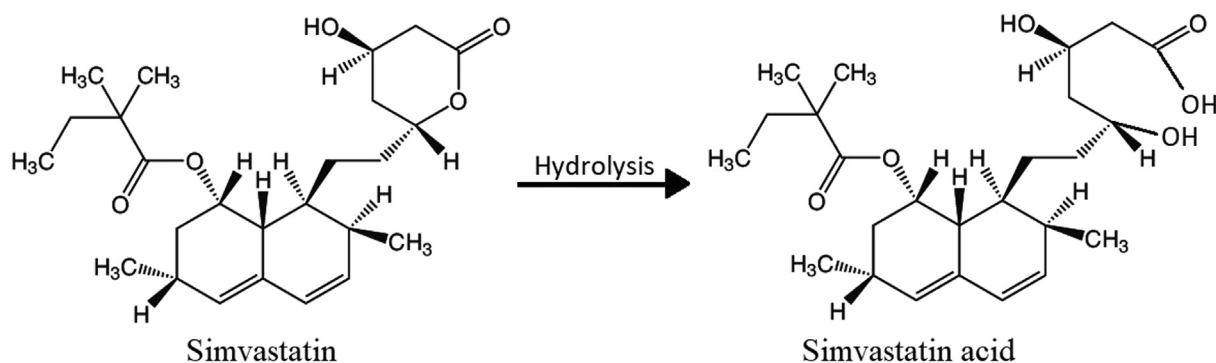

Fig. 1. Chemical structures of simvastatin and simvastatin acid.

The present study aimed to prepare SVCSChSNPs, which were assembled using the ionic gelation method and optimized using the Box-Behnken design. The optimized NPs were characterized physicochemically and pharmaceutically in terms of particle size, zeta potential, morphology, and *in vitro* release. The intracellular localization of anti-apoptotic properties of the formulated NPs was investigated using confocal fluorescence microscopy and annexin V-fluorescein isothiocyanate, respectively. Moreover, the cytotoxicity of SVNPs against hepatoma cell lines (HepG2) as a surrogate model for hepatocellular carcinoma (HCC) was investigated. Besides, the pharmacokinetics parameters of the formulated NPs were studied in Wister albino rats. A factorial experimental design was adopted in this study to clarify the interaction between the formulating variables and save resources.

2. Materials and methods

2.1. Materials

The simvastatin (SV) used in this study was a generous gift from the Riyadh Pharma Co., Saudi Arabia. Low-molecular-weight chitosan (viscosity 20,000 cps) (degree of deacetylation [DD] of 92%), chondroitin 4-sulfate sodium salt (ChS, sodium content 5.6% w/w, molecular weight 59 kDa), simvastatin hydroxy acid ammonium salt sodium (SVA), lovastatin, lovastatin hydroxy acid sodium salt, rhodamine B isothiocyanate (RBITC), and carboxymethylcellulose were purchased from Sigma Aldrich Chemical Co. Ltd. (St. Louis, MO, USA). Sodium tripolyphosphate (TPP) and glacial acetic acid were obtained from BDH Organic (Poole, Dorset, UK). Ethanol, methanol, acetonitrile, and phosphoric acid (HPLC grade) were obtained from Fisher Scientific Co., (Loughborough, UK). phosphate buffer solution (PBS) (pH 7.4) solution (8 g NaCl (137 mM), 0.2 g KCl (2.7 mM), 1.15 g $Na_2HPO4\cdot\cdot7H_2O$ (8.1 mM), and 0.2 g KH_2PO_4 (1.47 mM) in 1000 mL deionized water. Deionized water was obtained using a Milli-Q® water purifier (Millipore, France) and used throughout the study.

2.2. HPLC assay of simvastatin for in vitro studies

The SV concentration of all *in vitro* experiments was quantified using a Waters HPLC system (USA) equipped with a Waters RP C18 analytical column (5 μm × 4.6 mm ID × 150 mm). An isocratic elution method was involved, with a mobile phase comprised of methanol and water with 0.05% acetic acid (85:15) at a flow rate of 1.2 mL/min. The eluent was monitored at an ultraviolet detection wavelength of 238 nm. Linear calibration curves ($R^2 \geq 0.998$) were obtained by plotting the chromatographic peak area against SV concentration over a range of 0.2–10 μg/mL.

2.3. Experimental design

In this study, a three-factor, three-level Box-Behnken experimental design (BBD) was used to optimize the SVCSChSNPs nanoformulations. The three independent factors were CS solution concentration (X_1), the mass ratio of CS:ChS (X_2), and the pH of CS solution (X_3), while particle diameter (Y_1), polydispersity index (PDI) (Y_2), ZP (Y_3), and Higuchi model slope (Y_4) were the dependent variables (Table 1). The independent factors and their levels (expressed as low, −1; medium, 0; high, +1) were selected based on the results of a preliminary experimental screening study. Fifteen runs of SVCSChSNPs were suggested by Statgraphics® Centurion XVII.II software (StatPoint Technologies, Inc. Virginia, USA). The results of the BBD were evaluated using analysis of variance (ANOVA), with significance set to $P < 0.05$, and graphical analysis

Table 1
Experimental variables, their levels, and desirability of dependent responses.

Independent factors	Levels		
	Low (1-)	Medium (0)	High (1)
X_1 = CS solution concentration (mg/mL)	0.2	0.35	0.5
X_2 = CS:ChS mass ratio (w:w)	1:4	2.125:1	4:1
X_3 = pH of CS solution	3.5	4.25	5

Dependent variables	**Constrains**
Y_1 = Particle size (nm)	Minimize
Y_2 = Polydispersity index	Minimize
Y_3 = Zeta potential (mV)	Maximize
Y_4 = Higuchi model slope	Minimize

using the Pareto chart to determine the potential interactive factors.

2.4. Production of SVCSChSNPs

SVCSChSNPs were fabricated using the ionic gelation technique (Calvo et al., 1997), with a few modifications. Briefly, CS stock solution (1 mg/mL) was created by dissolving CS in 50 mL 1% (w/v) acetic acid while stirring 25 °C for 4 h. The solution was adjusted for pH at a specified value using 1 N NaOH and then passed through a 0.45 μm membrane to remove the insoluble parts. TPP solution was produced separately at a concentration of 0.03% w/v and mixed with ChS solution. In a 1.5 mL tube, SVCSChSNPs were synthesized by dropping 200 μL SV ethanolic solution (0.25 mg/mL) followed by 200 μL ChS-TPP mix into 600 μL CS solution and then mixed by pipetting up and down for a few minutes. The obtained NPs were filtered and centrifuged at 5000 rpm at 4 °C for 30 min using an Optima™ Max-E Ultra Cooling Centrifuge (Beckman Coulter, Pasadena, CA). The NPs in the supernatant were separated using a freeze dryer (Alpha 1-4LD Plus, Martin Christefrier trocknugsanlagen GmbH, Osterode am Harz, Germany) at − 60 °C for 48 h. The lyophilized NPs were collected for further evaluation. Void CSChSNPs were formulated as described previously without adding the drug. The NPs were produced and analyzed three times according to the experimental design.

2.5. Evaluation of particle size, polydispersity, and zeta potential

The particle size and PDI of each batch of the SVCSChSNPs were assessed using photon correlation spectroscopy by a Zetasizer Nano ZS (Malvern Instruments, UK). The monodisperse samples were diluted with deionized water and sonicated for 5 s to remove air bubbles and split aggregates. The samples were assessed at room temperature using a dynamic light scattering procedure at a 90° scattering angle. To determine the surface charge, the same Nano ZS was set to laser doppler velocimetry mode at 25 °C. All samples were measured in triplicate, and the results were expressed as the mean ± standard deviation (SD).

2.6. In vitro release profile and kinetic modeling

The SV release from each run of the SVCSChSNPs was evaluated using the dialysis bag diffusion method (Harisa et al., 2017), with some modification. The dialysis membranes (MWCO of 12 kDa, Sigma Aldrich, US) enclosing SVCSChSNPs (equivalent to 5 mg SV) were immersed in the flasks of the USP Dissolution Apparatus 2 (Caleva Ltd., Model 85 T, Philips, UK), keeping the paddle rotated at 50 RPM. The dissolution medium was 500 mL 0.1 N HCl (pH 1.2), maintained at 37 °C, and gradually raised by adding 0.05 M PBS (pH 8.0) dropwise to pH 7. At predetermined time intervals (0.1, 0.16, 0.3, 0.5, 1, 2, 4, 6, and 8 h), 5 mL aliquots were withdrawn

and instantly compensated with fresh medium. The samples were analyzed for SV concentration using the HPLC method. The release profile data on the SV from CSChSNPs were fitted to mathematical release models: zero, first-order, Higushi diffusion, Korsmeyer–Peppas, and Hixon-Crowell cube root law. To select the preferred model, the correlation coefficient was calculated for each mechanism. Models with the highest values were more likely to be chosen as the best model. In addition, the dissolution mechanism was determined by calculation of the exponent (n) values.

2.7. Prediction, synthesis, and evaluation of the optimized formula

The data obtained from the 15 batch evaluations of the SVCSChSNPs were analyzed using Statgraphics software, and an optimized value of each independent parameter was chosen to predict the optimized formulation. The predicted formulation was produced, assessed for all responses (i.e., Y_1–Y_4), and compared with the values predicted by the BBD.

2.8. Entrapment efficiency and drug loading

The quantity of SV incorporated in the optimized SVCSChSNPs was estimated through the ultracentrifugation method. Approximately 2 mg of prepared NPs was ultra-centrifuged with ethanol at 35,000 for 30 min at 4 °C using an Optima™ Max-E Ultra Centrifuge, and the supernatant was collected. Next, the non-encapsulated drug content was quantified by HPLC assay. The entrapment efficiency (EE%) and the drug loading (DL%) were calculated by Eq. (1 & 2) respectively.

$$EE\% = \frac{SV_{total} - SV_{free}}{SV_{total}} \times 100 \qquad (1)$$

$$DL\% = \frac{Amount\ of\ encapsulated\ SV}{Total\ weight\ of\ SVCSChSNPs} \times 100 \qquad (2)$$

SV_{total} is the quantity of drug added, while SV_{free} is the free quantity of drug that appeared in the supernatant.

2.9. Transmission electron microscopy (TEM)

The shape and particle size of the CSChSNPs and SVCSChSNPs were characterized using transmission electron microscopy (TEM). The sample was prepared by positioning one drop of monodisperse NPs onto a glow-discharged carbon-coated grid for 5 min. Then, the sample was rinsed with 15 drops of distilled water and stained with 1% uranyl acetate stain. Afterward, the grid was dried and examined by TEM using a JEM-1011 microscope at 80 kV accelerating voltage (JEOL, Tokyo, Japan).

2.10. X-ray powder diffraction

To investigate the physical interaction between SV, CS, ChS, and TPP, the X-ray diffraction of SV, CS, ChS, and TPP powders as well as the CSChSNPs and SVCSChSNPs was evaluated using an Ultima IV diffractometer (Rigaku Inc., Japan) with Cu as the tube anode. The samples were analyzed between 3 and 60 (°2θ) at a scan speed of 0.5 deg·min^{-1}. The tube anode was Cu with Ka = 0.1540562 nm monochromatized with a graphite crystal. The diffractograms were gathered at a tube voltage of 40 kV and a tube current of 40 mA in step scan mode (step size 0.02°, counting time 1 s per step).

2.11. Thermal scanning

Differential scanning calorimetry (DSC) was performed to detect the thermal curves of pure SV, CS powder, ChS powder, CSChSNPs, and the optimal SVCSChSNPs using a Shimadzu DSC-60 (Shimatzu Corporation, Tokyo, Japan). Approximately 4 mg of the sample was loaded in small aluminum pans and crimped. The thermograms were observed over a temperature range of 25 °C–300 °C at a heating rate of 10 °C min^{-1} under nitrogen gas. A sealed pan with no sample was used as a blank.

2.12. Fourier transform infrared spectroscopy

The Fourier transform infrared (FTIR) spectra of pure SV, CS powder, ChS powder, CSChSNPs, and the optimized SVCSChSNPs were acquired by using an FTIR spectrometer (Shimadzu® Europe – Prestige-21) via the potassium bromide (KBr) disc method. Approximately ~4 mg of sample and KBr were combined, compressed into small disks using a manual hydraulic press, and then scanned from 5000 to 400 cm^{-1}.

2.13. In vitro release study and kinetic modeling

The SV release behavior of the pure SV suspension and optimized SVCSChSNPs was evaluated using the dialysis bag diffusion method (Harisa et al., 2017) with some modification. The procedures were conducted as shown in section 2.6.

2.14. HepG2 cell culture

Human hepatocellular carcinoma cells (HepG2 cells) obtained from the American Type Cell Culture (ATCC, USA) were allowed to grow in T-75 flasks and then incubated in a humidified incubator at 37 °C with 95% air/5% CO$_2$ supplemented with Dulbecco's modified Eagle's medium (DMEM; Gibco, Grand Island, NY) enriched with 10% (v/v) fetal bovine serum (Gibco). The DMEM was changed every 24–48 h until a complete sheet was obtained. The cell layers that appeared were detached by trypsin-EDTA. Sterile PBS was used to wash and separate the old media. Approximately 0.5–1 mL of trypsin-EDTA solution was added to the cell monolayer, and the cells were incubated for 3–4 min. After the incubation period, the cells were collected and mixed with fresh culture medium for counting. In a 96-well microplate, HepG2 cells were seeded at a density of 1×10^4 cells/well and incubated at 37 °C in 95% humidified air and 5% CO$_2$ overnight for complete adhesion (Wang et al., 2019).

2.15. MTT assay

An MTT assay using HepG2 cells was performed to evaluate the cytotoxicity activity. In the test, the mitochondria of viable cells convert hydrophilic tetrazolium salt (yellow color) into a hydrophobic purple dye known as formazan, and the intensity of the dye is directly proportional to the number of surviving cells (Wang et al., 2019). In 96-well plates, freshly prepared samples with concentration dispersions corresponding to 0.5, 1, 2.5, 5, 10, 25, 75, 100, 125, 150, 175, and 200 μg of pure SV suspension, CSChSNPs, and the chosen SVCSChSNPs were passed through 0.450 μm syringe filters. These samples were incubated with previously cultured cells for periods of 24, 48, and 72 h. After the incubation period, the media were then eliminated from the wells to abort uptake, and the cells were washed with fresh media. A 50 μL aliquot of MTT (0.42 mg/mL) was added to each well, and the microplate was returned to the incubator for 4 h. After incubation, the media was removed, the MTT was solubilized in 1 mL of isopropyl alcohol, and the absorbance of each sample was mea-

sured at 570 nm using a microplate reader (ELX 800; Bio-Tek Instruments, Winooski, VT, USA).

Cell viability was determined by Eq. (3):

$$Cell\,viability\% = \frac{Absorbance_{sample}}{Absorbance_{control}} \times 100 \tag{3}$$

2.16. Flow cytometry analysis

HepG2 cells were assayed for apoptosis against concentrations of pure SV suspension, CSChSNPs, and SVCSChSNPs corresponding to their IC_{50} values using an annexin V-fluorescein isothiocyanate (FITC)/propidium iodide (PI) apoptosis detection kit I (Sigma, USA), according to the manufacturer's protocol. Briefly, cells were seeded into 12-well plates at a density of $\sim 1 \times 10^6$ cells/well in 1 mL DMEM for 12 h. Concentrations of 28.15 μg/mL, 63.85 μg/mL, and 3.67 μg/mL of pure SV suspension, CSChSNPs, and SVCSChSNPs, respectively, were added to the cell lines and then incubated for 24 h. The cells were then washed with PBS and digested with trypsin. Next, the cells were harvested by centrifugation at 2000 × g. Subsequently, cells were diluted by 5 × binding buffer with double distilled water, and 500 μL of suspension cells with 1 × binding buffer were prepared. Next, 500 μL of treated and the non-treated cell suspension was incubated with 5 μL of Annexin V-FITC and 10 μL of PI at room temperature for 30 min in darkness. The fluorescence of the cells immediately was measured using a flow cytometer (Beckman Coulter, CA, USA) (Wang et al., 2019). The rates of apoptosis were calculated as (cell numbers in Q2 + Q3/total cell numbers) × 100% (cells in Q2 were referred to as late apoptosis, in Q3 were referred to as early apoptosis).

2.17. In vitro ASGPR-mediated intracellular uptake

The intracellular localization of the obtained nano delivery system was detected using a confocal laser microscope (Nikon Eclipse 90i, Nikon Corporation, Tokyo, Japan) after labeling the CS with rhodamine B isothiocyanate (RBITC) (Jiang et al., 2017).

2.17.1. Production of RBITC-labeled CS

RBITC-labeled CS was manufactured by dissolving 250 mg of CS in 10 mL of acetic acid (1%, w/v) and mixing it with 2.5 mg RBITC. The mixture was left to react for 12 h and then dialyzed against deionized water for 3 d. RBITC-CS coagulates in water and can be collected by centrifugation and subsequent lyophilization using freeze-drying. The dye-grafted CSChSNPs were fabricated by the aforementioned method using the modified Calvo method (Calvo et al., 1997).

2.17.2. Fluorescence analysis

To detect the intracellular uptake of the optimized SVCSChSNPs, hepatocarcinoma cells were subcultured on 8-well chamber slides (Lab-Tek II Chamber Slides; Thermo Fisher Scientific Inc, USA) at a density of 1×10^4 cells/well for 24 h. After this period, the cells were washed three times with PBS to remove the medium before adding the NPs. The dye-labeled nanocarriers were dispersed in 10 mL medium and 500 μL was added to each well. NPs were added in the absence and presence of aqueous galactose 65 mM preincubated with the cells for 1 h. After that, the cells were incubated at 37 °C and 5% CO_2 for 4 h, washed using PBS to remove the medium, and fixed with 5% paraformaldehyde in PBS for 30 min, and then observed by confocal microscopy. Control cells were incubated with deionized water, washed with PBS, and fixed as before. The cell nuclei were stained with Hoechst 33,258 (blue, 5 mg/mL) for

30 min at 25 °C and imaged using a confocal microscope (Pranatharthiharan et al., 2017).

2.18. In vivo pharmacokinetic study

An oral pharmacokinetic study was performed on 12 male Wistar rats in a fasted state over a 12 h period. All animal experiments were approved by the Animal Ethics Committee, College of Pharmacy, King Saud University, under reference number: KSU- SE-19–58. Animals were sourced from the Animal House (College of Pharmacy, King Saud University). Each one weighed 200–250 g at 12 weeks of age. Water was provided *ad libitum* throughout the study.

The animals were divided into two groups of six animals each: the standard group and test group, which received a single dose of 0.5 mL SV suspension or SVCSChSNPs dispersed in sterile water (at SV equivalent to 20 mg/kg body weight) via oral gavage, respectively. The dose of 20 mg/kg body weight is the dose at which SV acts as an antiproliferative agent (Muscella et al., 2014; Wang et al., 2017) .The drug suspension was produced by dispersing the pure SV powder in sterile water containing 0.25% (w/v) sodium carboxymethylcellulose with sonication for 10 min. After dosing, 200 μL blood samples were collected in pre-heparinized polyethylene tubes from the central tail vein at predetermined time points of 0.5, 1, 2, 4, 6, 8, and 12 h. The samples were immediately centrifuged at 3500 rpm for 5 min at 24 °C, and the plasma was separated and stored at − 20 °C for further analysis.

2.18.1. HPLC analysis

The SV and SVA content was quantified using the HPLC method as previously reported (Rizvi et al., 2019; Silva et al., 2012). The internal standards were lovastatin and lovastatin acid for SV and SVA, respectively. An HPLC system (Waters, Boston, Mass., USA) was equipped with a Waters 717 plus autosampler, Waters 1525 binary HPLC pump, Waters 2487 dual ë absorbance detector, RP C18 Waters column (5 μm × 4.6 mm ID × 150 mm). The mobile phase was comprised of acetonitrile and deionized water (65:35%, v/v) adjusted to pH 3.5 using phosphoric acid at a flow rate and injection volume of 1.0 mL/min and 20 μL, respectively. The eluent was monitored with a UV detector at a wavelength of 238 nm. These parameters resulted in SV and SVA retention times of approximately 7 and 6.2 min, respectively. Linear calibration curves ($R^2 = 0.998$ and $R^2 = 0994$ for both SV and SVA, respectively) were obtained by plotting the peak area ratio of analyte: internal standards against the known concentrations. The limit of quantification for both SV and SVA was found to be 5 ng/mL and 10 ng/mL, respectively.

2.18.2. Pharmacokinetic analysis

The PK parameters of SV and SVA were calculated using the PK solver program (Zhang et al., 2010). The parameters employed an area under the plasma concentration–time curve up to time infinity ($AUC_{0\rightarrow\infty}$), the area under the curve (AUC_{0-12}), the maximum plasma concentration (C_{max}) the time required to reach the maximum plasma concentration (T_{max}), the elimination half-life ($T_{1/2}$), the mean residence time (MRT_{0-12}), the volume of distribution during the terminal phase (Vz/F), and the total body clearance (Cl/F). The relative bioavailability was determined relative to pure SV suspension. All data were represented as the mean ± SD.

2.19. Statistical analysis

All experiments were conducted in triplicate (n = 3), and the data were expressed as means ± SD. The significance of the formulation factors was evaluated using one-way ANOVA. Pharmacokinetic parameters were analyzed by PK Solver software using a

non-compartmental model. Tukey's multiple comparisons test was conducted using the SPSS program to assess statistical differences ($P < 0.05$) between the group means. The results were expressed as means ± SD.

3. Results and discussion

The present study produced ultrafine SV nanocarriers from biodegradable polymers CS and ChS using straightforward formulation procedures under mild production conditions. The intended SVNPs were designed to reach their final destination using dual-mechanism targeting: passive targeting (the EPR) through the production of NPs with particle size <100 nm and active targeting using ASGPR-mediated endocytosis. Part of the aim of the study was to enhance the oral bioavailability of the SV and repurpose it as an anticancer agent. The SVNPs were assembled using the ionic gelation technique. This technique involves straightforward procedures with mild production conditions. The formulation conditions were optimized using BBD to fabricate reproducible NPs, which can save time as well as resources. The optimized formulation was characterized by its physicochemical properties, *in vitro* SV release behavior, and kinetic modeling of the release profiles. An *in vitro* biological evaluation was conducted to determine the cytotoxicity, induction of apoptosis in HepG2 cells, and intracellular localization in HCC. The *in vivo* bioavailability of the SVNPs was also assessed using Wister albino rats.

In the present study, fifteen runs were successfully fabricated and evaluated, and the obtained data were analyzed to optimize the processing factors. SVCSChSNPs were assembled by electrostatic attraction between carboxylate and sulfate groups from ChS and phosphate groups from TPP on one hand and amino groups of CS on the other hand to form a polyelectrolyte complex. The particle size of the NPs oscillated between 47 ± 0.56 nm in F2 and 177 ± 1.62 nm in F12, while the PDI oscillated between 0.112 ± 1.44 in F5, F 6, and F13 and 0.576 ± 2.87 in F9. All formulations exhibited cationic ZP values oscillating between 25 ± 0.22 mV in F1 and F4 and 33 ± 0.75 mV in F14 (Table 2). The Higuchi release constant ranged from 12 ± 1.63 in F12 to 17 ± 0.22 in F10. Similarly, Soe et al. produced CS/ChS NPs conjugated with folic acid and loaded with bortezomib. The particle size and PDI values of bortezomib Cs/Chs folic acid NPs were 196.5 ± 1.2 nm and 0.21 ± 0.5, respectively (Soe et al., 2019). Also, in another study, nanosized CS/ChS particles were fabricated with diameters, PDI,

surface charge, and drug values of 283.2 ± 16 nm, −31.2 ± 6.8 mV, 63.1% ± 4.2%, and 6.14 ± 0.3 h, respectively (Rezazadeh et al., 2019).

The *in vitro* release profiles of the SV from the fifteen CSChSNPs runs showed a two-phase release pattern after 12 h. The pattern includes an initial fast release followed by a steady release phase. All release data were fitted to various kinetic models and were found to obey the Higuchi kinetic model (data not shown).

3.1. Assessment of the quantitative effects of the processing factors

3.1.1. Influence of chitosan solution concentration
From the data shown in Table 3 and Fig. 2, we found that the concentration of the initial CS solution (X_1) had a significant synergetic effect on Y_1, with a P-value of 0.0102. The quadric term of X_1^2 exerted a significant synergetic influence on Y_2 (P-value = 0.0119).

As shown in Table 2, there were clear trends of an increase in particle diameter from 47 ± 0.56 nm to 119 ± 2.44 nm and an increase in PDI from 0.201 ± 1.21 to 0.502 ± 3.15 when the CS concentration in F2 and F10 increased from 0.2 mg/mL to 0.5 mg/mL. These findings are consistent with those of other studies (Rezazadeh et al., 2019). In CS solutions with low concentrations, the electrostatic forces between carboxylate, sulfate, and phosphate anions and the protonated amino groups of CS predominate over the attractive forces created by the intermolecular hydrogen bonding between CS molecules, which could explain the above trend. At higher CS concentrations, hydrogen bonding overcomes the electrostatic attraction, which results in greater particle size upon the addition of ChS and TPP; this is because more than one polymer molecule is used to produce an individual nanoparticle. The higher the CS concentration, the higher the density of protonated amine groups, causing greater repulsion among them and, accordingly, a growth in hydrodynamic diameter (Rezazadeh et al., 2019).

3.1.2. Influence of the weight ratio of CS to ChS
As shown in Table 3 and Fig. 2, the interaction between X_2 and X_3 had a significant synergistic influence on Y_2, with a P-value of 0.0450, and a significant antagonistic influence on Y_1, with a P-value of 0.0313. The quadric term of X_2^2 showed a synergetic influence on both Y_2 and Y_4, with P-values of 0.0115 and 0.0374, respectively. With increasing ChS amounts (mass ratio from 4:1 in F11 to 1:4 in F2), particle diameter decreased from 105 ± 0.93 nm to 47 ± 0.56 nm, particle distribution decreased from 0.452 ± 2.94

Table 2
The experimental runs and the values observed of the response variables.

Run	Factors			Responses			
	X_1	X_2	X_3	Y_1	Y_2	Y_3	Y_4
F1	0.2	2.125	3.5	102 ± 0.92	0.412 ± 2.62	25 ± 0.22	15 ± 1.63
F2	0.2	0.25	4.25	47 ± 0.56	0.201 ± 1.21	27 ± 0.31	16 ± 1.44
F3	0.5	2.125	3.5	128 ± 1.23	0.380 ± 2.11	27 ± 0.15	14 ± 1.83
F4	0.35	0.25	3.5	89 ± 0.82	0.521 ± 2.43	25 ± 0.24	16 ± 0.96
F5	0.35	2.125	4.25	68 ± 1.36	0.112 ± 1.44	30 ± 0.73	14 ± 0.42
F6	0.35	2.125	4.25	68 ± 1.36	0.112 ± 1.44	30 ± 0.73	14 ± 0.42
F7	0.35	0.25	5	159 ± 1.98	0.298 ± 2.35	31 ± 1.32	16 ± 0.74
F8	0.35	4	3.5	149 ± 1.76	0.398 ± 2.48	28 ± 1.45	13 ± 0.65
F9	0.35	4	5	96 ± 2.55	0.576 ± 2.87	29 ± 1.86	15 ± 0.73
F10	0.5	0.25	4.25	119 ± 2.44	0.502 ± 3.15	27 ± 1.65	17 ± 0.22
F11	0.2	4	4.25	105 ± 0.93	0.452 ± 2.94	29 ± 0.44	15 ± 1.4
F12	0.5	2.125	5	177 ± 1.62	0.498 ± 2.43	31 ± 0.66	12 ± 1.63
F13	0.35	2.125	4.25	68 ± 1.36	0.112 ± 1.44	30 ± 0.73	14 ± 0.42
F14	0.5	4	4.25	174 ± 1.83	0.511 ± 1.68	33 ± 0.75	15 ± 1.85
F15	0.2	2.125	5	109 ± 1.92	0.498 ± 1.45	32 ± 0.68	14 ± 1.66

Notes:
Data are expressed as the mean ± standard deviation (n = 3). Abbreviations Chitosan solution concentration (w/v), X1, Chitosan:Chondroitin sulfate mass ratio (w:w), X2, pH of chitosan solution, X3, Particle size (nm), Y1, PDI, Y2, Zeta potential (mV), Y3, Higuchi model slope, Y4

Table 3
Estimated effects and associated P-values for the response variables.

Source	Y1		Y2		Y3		Y4	
	Estimated Effect	*P*-value	Estimated effect	*P*-value	Estimated effect	*P*-value	Estimated effect	*P*-value
A:CS soln conc, X_1	58.75	0.0102*	0.08225	0.1838	1.0	0.2856	−0.5	0.5209
B:CS:ChS mass ratio, X_2	27.5	0.1195	0.104	0.1087	2.0	0.0624	−1.75	0.0605
C:pH of CS soln, X_3	18.25	0.2683	0.03975	0.4897	4.5	0.0030*	−0.25	0.7441
AA (X_1^2)	49.0	0.0723	0.303	0.0119*	−0.25	0.8471	0.5	0.6589
AB (X_1X_2)	−1.5	0.9451	−0.1215	0.1682	2.5	0.0883	−0.5	0.6462
AC (X_1X_3)	21.0	0.3575	0.016	0.8404	−1.5	0.2607	−0.5	0.6462
BB (X_2^2)	37.5	0.1427	0.3055	0.0115*	−1.25	0.3567	3.0	0.0374*
BC (X_2X_3)	−61.5	0.0313*	0.2005	0.0450*	−2.5	0.0883	1.0	0.3739
CC (X_2^2)	73.0	0.0196*	0.367	0.0055*	−2.25	0.1273	−1.0	0.3915

* Significant, p < 0.05

to 0.201 ± 1.21, and ZP decreased from + 29 ± 0.44 mV to + 27 ± 0.31 mV (Table 2). This observation could be attributed to the fact that by decreasing the ratio, the effect of ChS on the synthesis medium increased and more NH_3^+ groups were neutralized by the ChS negative charge, thereby overcoming the resistance of the CS molecules and ultimately decreasing the PDI. The colloidal PEC approach was formed at certain CS and ChS percentages where excess CS molecules increased the intermolecular attraction forces between CS molecules and resisted the electrostatic attraction force between ChS anions and NH_3^+ cations. As a result, the particle diameter was increased and the particle distribution was expanded.

3.1.3. Influence of the CS solution pH

As shown in Table 3 and Fig. 2, there was a positive correlation between X_3 and Y_3, with a *P*-value of 0.0030. The interaction between X_3 and X_2 had a significant antagonistic influence on Y_1, but had a significant synergistic effect on Y_2, with *P*-values of 0.0313 and 0.0450, respectively. The quadric term of X_3^2 displayed significant synergetic effects on both Y_1 and Y_2, with *P*-values of 0.0196 and 0.0055, respectively. Based on this finding, the zeta potential increased as pH increased. As shown in Table 2, by increasing the pH from 3.5 in F3 to 5 in F12, the zeta potential increased from + 27 ± 0.15 mV to + 31 ± 0.66 mV, particle size increased from 128 ± 1.23 nm to 177 ± 1.62 nm, and particle distribution increased from 0.380 ± 2.11 to 0.498 ± 2.43.

A probably explanation for this result is that when the pH value was 3.5, fewer NH_3^+ groups were available for the unlike-charge attraction with the carboxylate, sulfate, and phosphate groups. As a result, the NPs resisted being produced from non-protonated CS molecules, thereby enlarging the particle diameter with no uniform diameter distribution with low surface charge value. By increasing the pH value, more amino groups became protonated, thereby increasing the surface charge of the obtained formulation. Moreover, multiple anions ($P_3O_{10}^{5-}$, $HP_3O_{10}^{4-}$, $H_2P_3O_{10}^{3-}$, $H_3P_3O_{10}^{2-}$, and $H_4P_3O_{10}^{-}$) may be present in solution depending on the pH when TPP is dissolved in water, which is undesirable because they can competitively react with the protonated ammonium groups (NH_3^+) of chitosan solution (Hejjaji et al., 2018). Therefore, when the pH of TPP/ChS is close to 5.0, predominantly $H_2P_3O_{10}^{3-}$ (~67%) ions exist in the solution, which allows the production of nanoparticles with good crosslinking, small particle size, and less polydispersion.

3.1.4. Prediction, production, and assessment of the optimized SVCSChSNPs

Following data analysis, the process of SVCSChSNPs assembly was optimized using Statgraphics software. The suggested optimized NPs comprised a 0.29 mg/mL CS concentration, a CS/ChS ratio of 2.14, and a pH of 4.28 for the CS solution. This setting

was predicted to provide SVCSChSNPs with Y_1, Y_2, Y_3, and Y_4 values of 73.60 nm, 0.107, +29.80 mV, and 14.13 respectively. The optimized NPs were manufactured and evaluated. The reactions of this scattering were 83 ± 0.57 nm, 0.160 ± 0.36, +30 ± 0.42 mV, and 14.7 ± 32 for Y_1, Y_2, Y_3, and Y_4, aligning with the estimations of the predicted model.

The interaction of ChS (through —OSO3— ⁻ and —COO⁻ groups) and TPP ($H_2P_3O_{10}^{3-}$) with CS (using —NH3⁺ groups) formed CS-ChS nanoparticles with virus-like surfaces, thereby allowing increased mucus penetration (Wu, Shan, Zhang, & Huang, 2018). Particles near 80 nm in size are beneficial for many reasons; for example, they are not detected by the reticuloendothelial system, and they represent the optimal range for minimizing clearance. In particular, cationic-charged nanoparticles directly interact with the negatively charged plasma membrane of the cells and achieve intracellular trafficking. Moreover, nanoparticles with diameters of ~ 100 nm and surface charges greater than + 30 mV are more stable and do not aggregate (Bugnicourt and Ladavière, 2016). Furthermore, NPs with a particle size distribution<0.3 show uniform monodispersity (Calvo et al., 1997). These characteristics make the assembled SVCSChSNP model a promising platform for pharmaceutical applications, especially intracellular drug delivery. Moreover, these findings demonstrate the practicability of this advanced methodology for using BBD to construct SVCSChSNPs with uniform and stable physicochemical highlights.

3.2. The entrapment efficiency

The EE and drug loading of the optimized SVCSChSNPs were calculated by using 50 mg SV in the preparation of the optimized CSChSNPs. The EE and drug loading values were 71% ± 3.8% and 2.12% ± 1.32%, respectively.

3.3. Transmission electron microscopy (TEM)

TEM micrographs of the SVCSChSNPs revealed a well-separated morphology with a particle size < 100 nm, as shown in Fig. 3. The void CSChSNPs were spherical, while the SV-loaded polyelectrolyte monodisperse were oval. In addition, the loading of SV into the nanoparticles did not affect the resultant nanoparticles' integrity.

3.4. Differential scanning calorimeter

Thermograms of pure SV, CS, ChS, CSChSNPs and the SVCSChSNPs are shown in Fig. 4(A). The melting point of the pure SV was indicated by an intensive endothermic peak at 140.96 °C, which revealed the SV crystallinity (Harisa et al., 2017). The CS thermogram exhibited a broad peak at ~ 72 °C, indicating the loss of water adsorbed by CS, and an exothermic peak at ~ 313.3 °C,
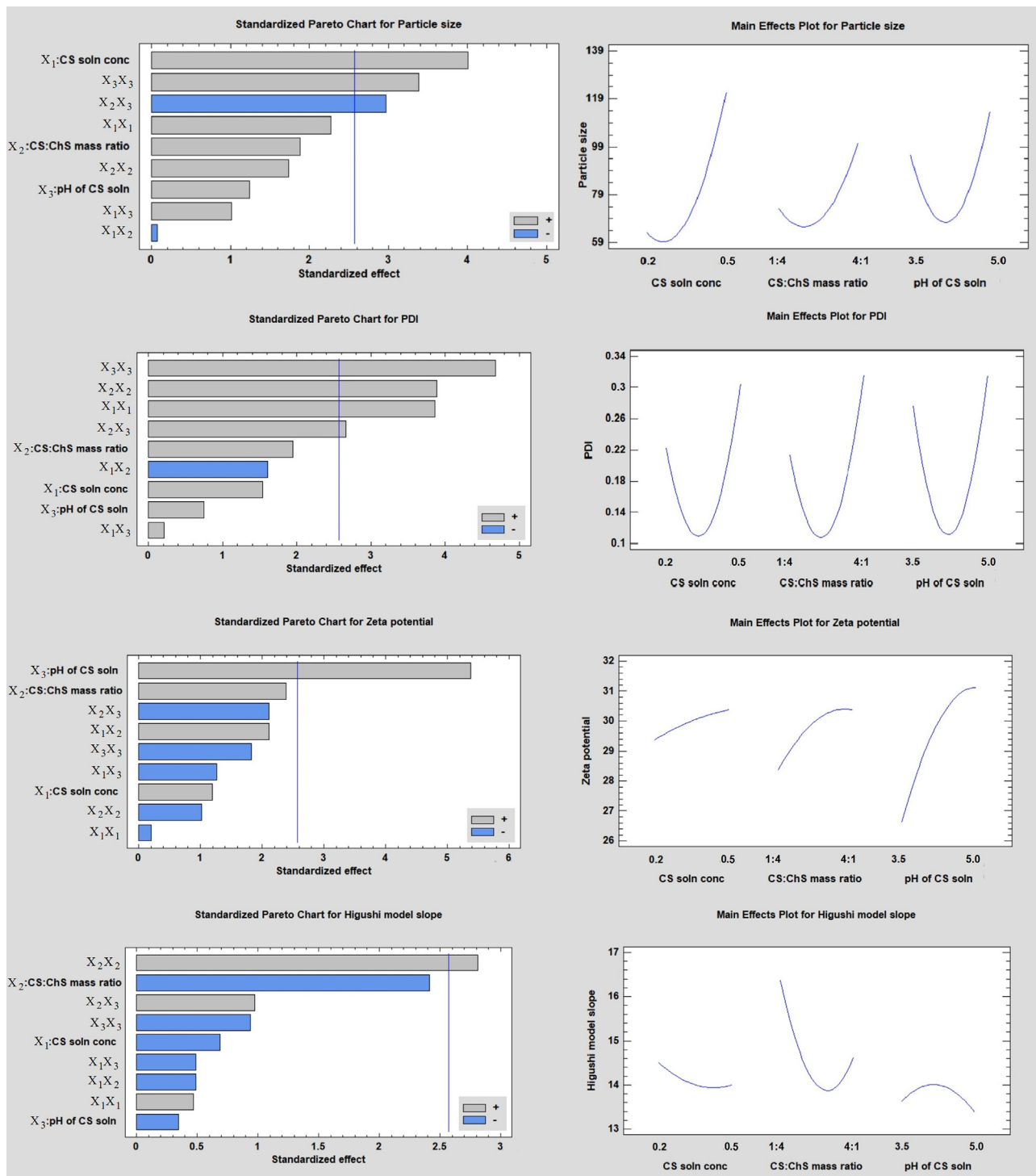
Fig. 2. Standardized Pareto chart and main effects plot for particle size, polydispersity index, zeta potential, and Higuchi model slope. **Abbreviations:** X_1X_2, X_1X_3, and X_2X_3 are the interaction patterns between the formulating factors, and X_1X_1, X_2X_2, and X_3X_3 are the quadratic patterns of the factors.

demonstrating the degradation of the polysaccharide. ChS displayed an endothermic peak at ~ 78 °C and a sharp exothermic peak at ~ 248 °C.

In the thermogram of CSChSNPs, an endothermic peak was observed at ~ 88 °C and an exothermic peak was observed at ~ 222 °C, indicating that NPs were successfully formed. In the case of the SVCSChSNPs, the degradation profile exhibited three endothermic peaks at 52 °C, 110 °C, and 226 °C corresponding to water molecule evaporation, SV degradation, and CS/ChS

matrix degradation, respectively. The peak of the SV appeared as a relaxed small peak, indicating the transformation from the crystal into a molecular structure. The interactions between CS and ChS groups impaired H-bonding. As a consequence, the polymer crystalline structures formed by H-bonding among the same polymer chains crashed. This suggests that the crystalline structure of the pure polymer may be modified or even destroyed due to the formation of CSChSNPs, which consequently alters its thermal behavior.
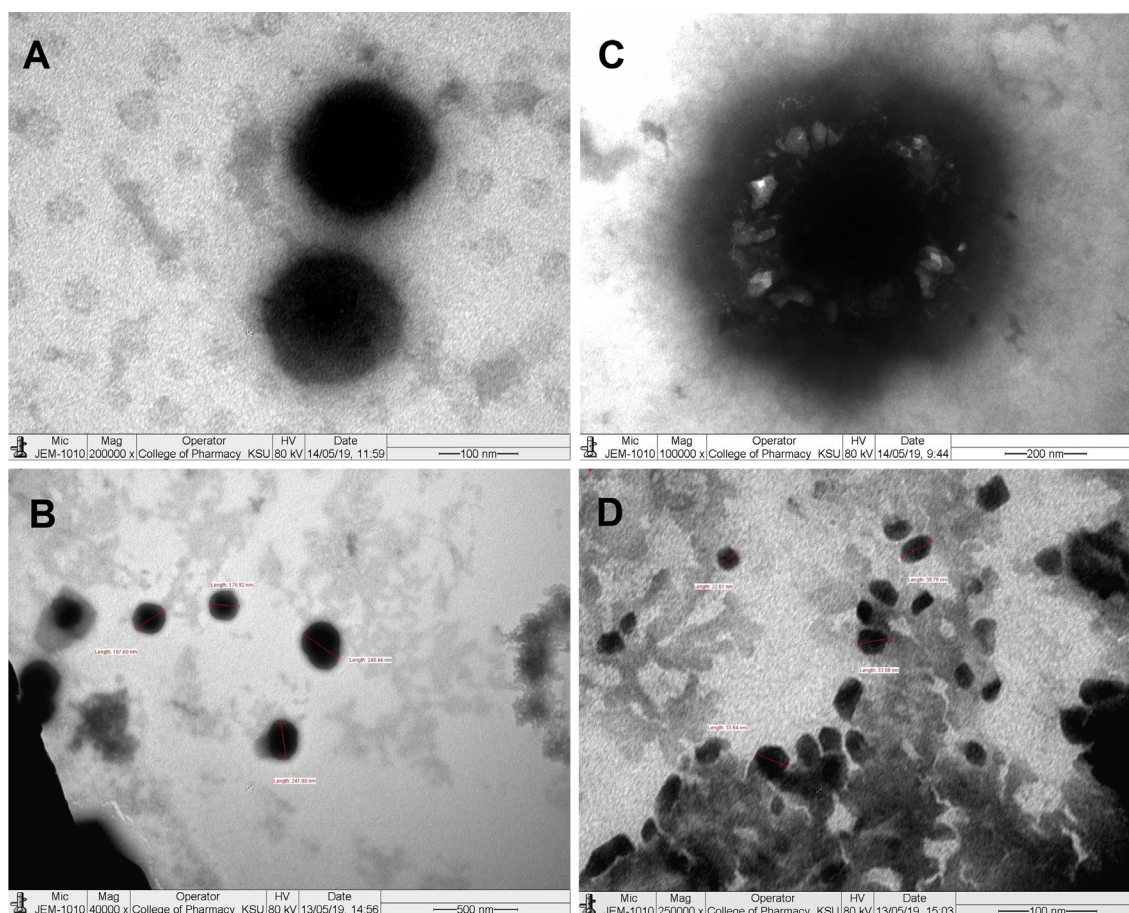
Fig. 3. TEM micrograph of (3A, 3B) the optimized void CSChSNPs and (3C, 3D) the optimized SVCSChSNPs.

3.5. Fourier transform infrared spectroscopy

Fig. 4(B) illustrates the FTIR spectra of the pure SV, CS, ChS, CS/ChS, and SVCSChSNPs. The identification peaks of the SV spectrum were observed at 3550 cm^{-1}, 2969.70 cm^{-1}, and 1707.37 cm^{-1}, corresponding to the O–H stretch, C–H stretch (alkane), and C = O stretch, respectively. The CS spectrum showed two overlapped wide N-H and − OH peaks at 3430 cm^{-1} and two other sharp signals at 1401 cm^{-1} and 1638.60 cm^{-1}, confirming amine and amide bonds, respectively. In the ChS spectrum, the characterization peaks were at 3429 cm^{-1}, –OH stretching; 1639 cm^{-1}, amide I bond; 1564 cm^{-1}, amide II band; and 1257–1038 cm^{-1}, S = O stretching. In the CSChSNP spectrum, a band appeared at 1064 cm^{-1} assigned to NH$_3$SO$_3$ stretching, suggesting an interaction between both CS and ChS and TPP to form a new polymeric matrix. Moreover, the vibration of the NH$_2$ appearing on the CS spectrum at 1590 cm^{-1} and on the ChS spectrum at 1569 cm^{-1} moved to 1546 cm^{-1}, demonstrating that the primary amine group appears in the NPs in a protonated form (NH$_3^+$).

Compared with CSChSNPs and the SV spectra, the IR spectrum of SVCSChSNPs is simply the combination of both CS/ChS and the SV, with a slight shift in the peak position of SV, indicating that the SV was encapsulated in the NPs without interaction with the CS/ChS matrix (Hu et al., 2012; Jardim et al., 2015).

3.6. X-ray powder diffraction

Fig. 4(C) shows the powder XRD spectra of the pure SV, CS, ChS, CSChSNPs, and SVCSChSNPs, respectively. X-ray patterns provide information about the inter- and intra-molecular interactions within the complex network. The SV diffractogram (a) showed the presence of many sharp peaks at 2θ values of 9.2°, 10.8°, 17.1°, 17.6°, 18.7°, and 22.5°, proving its crystalline structure (Harisa et al., 2017). The XRD pattern of pure chitosan showed a large peak at 10.6° and another peak at 19.9°. The XRD of pure ChS showed a broad and low-intensity diffraction reflection at 2θ = 23.42°, indicating that ChS has a backbone with a low crystalline pattern.

In the CSChSNPs, the intensity of CS peaks was diminished, indicating that there was a significant decrease in CS crystallization on the CSChSNPs. A possible explanation may be the influence of the CS/ChS complex on flexibility in the overall polymer matrix, which suppressed the crystal growth of CS. In the XRD pattern of SVCSChSNPs, the intensive characterization peaks of SV were diminished and others peaks disappeared, demonstrating a less-crystalline form than that of the raw SV. This was probably due to the conversion of SV into an amorphous dispersion inside the polymeric NS matrix. The results of PXRD were consistent with DSC, suggesting that SV presents in the amorphous phase in the nanoparticle matrix.

3.7. Two-stage dissolution study

Fig. 5 shows the *in vitro* release profile of the pure SV suspension and optimized SVCSChSNPs. The SV suspension showed the lowest amount of dissolution over the 8 h period, reaching a maximum of 29.5%, as a result of its poor water solubility. Such observed improvement may be due to the carboxymethylcellulose
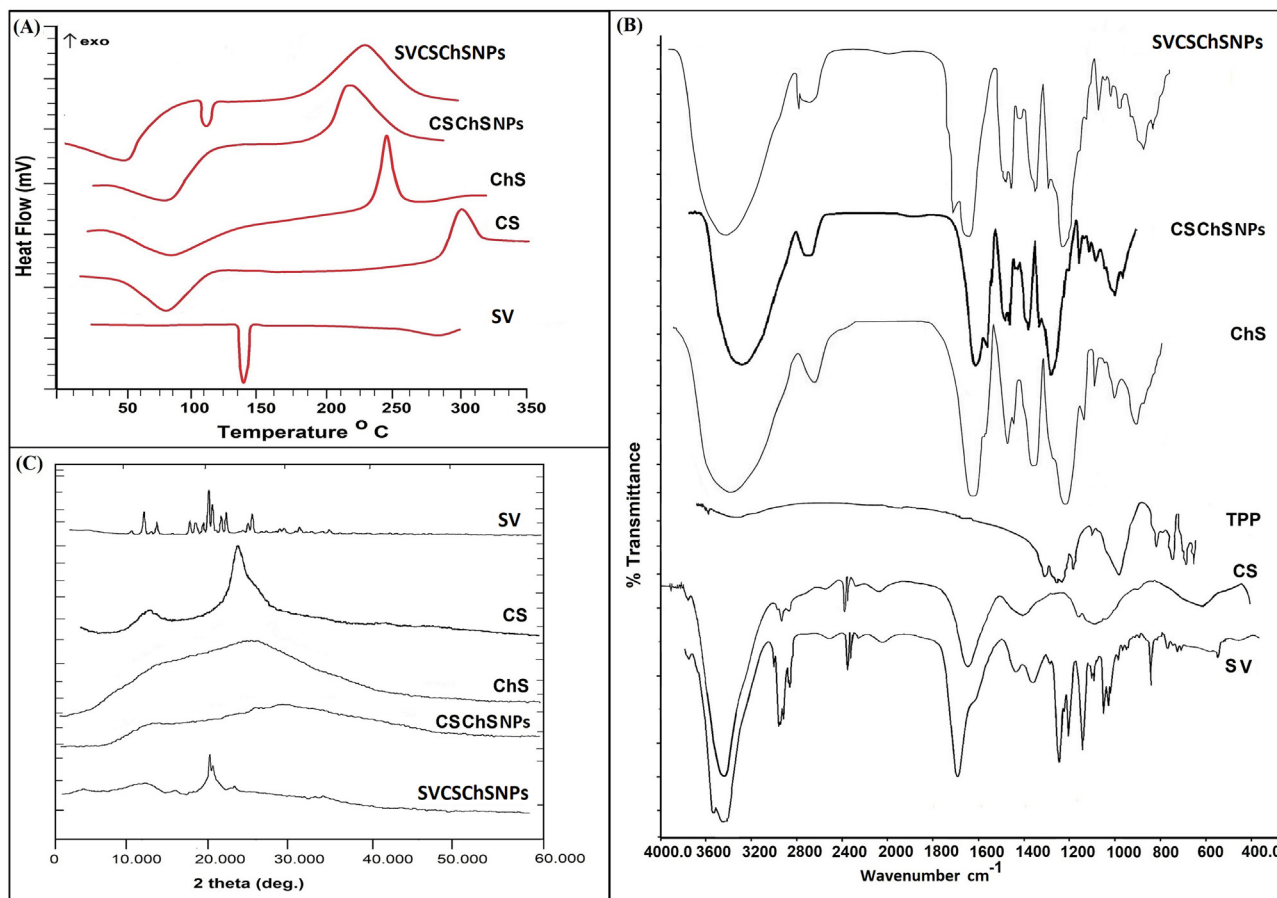
Fig. 4. (A) Thermograms, (B) FTIR spectra, (C) powder XRD spectra of the pure SV, CS, ChS, CSChSNPs and SVCSChSNPs.

used in the preparation of the pure drug suspension, which facilitates drug dissolution. In the case of the optimized NPs, after 8 h, a two-phase release pattern was observed, including an initial burst and fast release followed by a steady release phase. The two-phase release pattern reached a dissolution concentration up to 2.2-fold

greater than that of the free drug suspension. The initial phase continued for up to 2 h at pH 1.2, and during this period it released approximately 32.1% of the SV content. At pH 7, the fast release continued for up to 2 h, and during this period, the released SV amount was 64.21%. The release of SV in the first 2 h might be
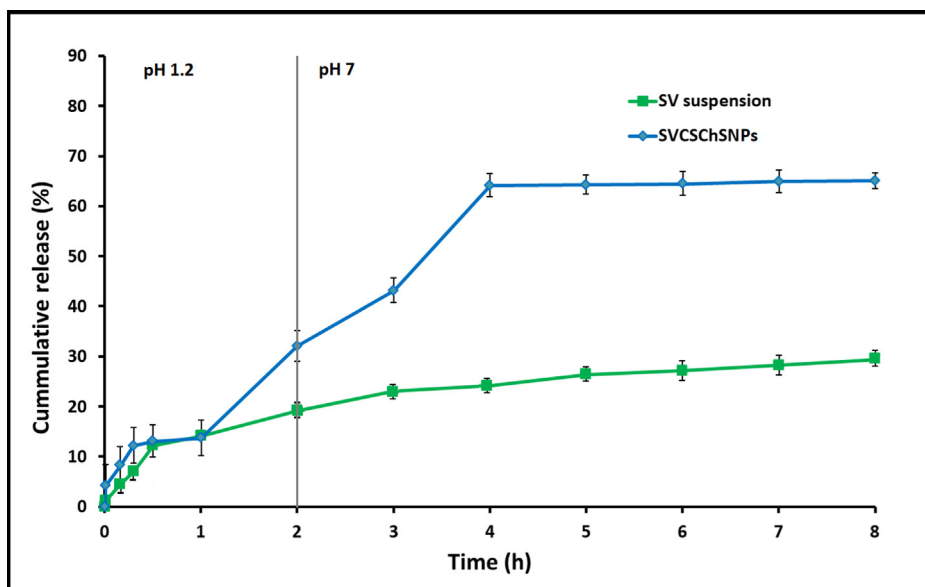

Fig. 5. The *in vitro* release profile of pure SV suspension and SVCSChSNPs at pH 1.2 and pH 7. Each value represents the mean ± SD; n = 3.

related to the flux of the fast dissolution of the SV moving from the surface of the loaded CSChSNPs to the release medium. Furthermore, the large surface area of the CSChSNPs maximized the amount of the liberated drug into the buffer medium. The slow-release phase liberated the SV at a decelerated rate, which might contribute to the diffusion of the entrapped drug inside the cross-linked matrix of the polymer. The amount of the released SV was directly proportional to the EE% of the SVCSChSNPs. The release behavior of SV from the optimal SVCSChSNPs was fitted to various kinetic models, including zero, first-order, Higuchi, Kors-meyer–Peppas, and Hixon-Crowell. The best fitting mathematical model was the Higuchi model (R^2 = 0.971). This result is consistent with other studies showing that the CS/ChS matrix can control the release of a drug through a two-phase release pattern (Abdullah et al., 2016; C.-S. Hu et al., 2014; Jardim et al., 2020; Umerska et al., 2017). The addition of small amounts of ChS increases the crosslinking and the mechanical strength of CS/TPP NPs (Yuan et al., 2008). The overall release data indicate the potential of CS/ChS to release entrapped SV in a controlled manner.

3.8. Cytotoxicity study on HepG2

The *in vitro* cytotoxicity of free SV suspension, CSChSNPs, and SVCSChSNPs against HepG2 cells was investigated using the MTT assay at 37 °C. SV is used to reduce hyperlipidemia. Many studies discussed its activity on proliferation, where this process is involved in cancer development. Alkhatib and Al-Merabi (2014) investigated the activity of SV on HCC using HepG2 cells model. Sedki et al (2018) examined effects of SV on human prostate cancer cell line (PC-3). In the current study, as shown in Fig. 6, the cell viability of HepG2 cells decreased with increasing sample concentration, indicating dose-dependent cytotoxicity. The toxicity effect was higher for SVCSChSNPs compared to the SV suspension and non-medicated CSChSNPs. The IC_{50} of SVCSChSNPs was significantly decreased to 3.67 µg/mL (*P* < 0.05) as compared with free SV, as shown in Table 4. The enhanced and specific toxicity of SVCSChSNPs on the HepG2 cell line could be attributed to the enhanced cellular internalization of SVCSChSNPs, as GalNAc present on their surface acts as a ligand for the ASGPRs overexpressed

in hepatoma cells. At the same time, the cellular uptake of SV suspensions without GalNAc in their formulation was reduced, resulting in reduced cytotoxicity. Moreover, the increased cytotox-icity of SVCSChSNPs could be due to the synergistic effect of CS and SV. In addition, cationic charge of the obtained NPs may enhance drug influx inside the tumor cell model (Harisa et al., 2016). The finding proved the efficacy of the engineered SVCSChSNPs against the *in vitro* HCC model. Similar studies have demonstrated that SV shows cytotoxicity against HepG2 cells *in vitro* (Relja et al., 2010).

3.9. Apoptosis assay of HepG2

Cell apoptosis induction was quantified after exposure to the IC50 values of CSChSNPs, free SV, and SVCSChSNPs, which were 63.85, 28.15, and 3.67, respectively, as shown in Fig. 7. After 24 h of treatment, a difference in early apoptosis and late apoptosis of control HepG-2 cells and treated HepG-2 cells was observed. Control cells showed 2.67% ±0.31%, 3.73% ±0.43%, and 3.93% ±0.38% early and late apoptosis, respectively, while IC50-treated cells showed significantly increased early and late apoptosis at 11.2 % ± 0.46%, 21.2% ±0.34%, and 33.34% ±0.36% for CSChSNPs, free SV, and SVCSChSNPs, respectively, (P < 0.05). The control cells were not stained with any dye, indicating that these cells were viable. The cells treated with the loaded formulation showed a green flu-oresce resulting from staining with annexin-V-FITC but not with PI, which indicates the incidence of apoptosis with no noticeable necrotic effect. The apoptotic action damaged the cell surface and released phosphatidylserine (Alkhatib & Al-Merabi, 2014). Wang et al. (2017) demonstrated that SV causes cell cycle arrest in HCC at the G0/G1 phase by induction of p21 and p27 accumulation in tumor section through reducing Skp2 expression and inducing AMP-activated protein kinase (AMPK) activation and signal trans-ducer and activator of transcription 3 (STAT3) suppression in the same tumor tissues. These findings suggest that SVCSChSNPs could initiate an apoptotic response in HepG-2 cells. They also suggest that statins induce apoptosis through interference cholesterol nec-essary for cellular and mitochondrial membrane stability (Y. C. Li, Park, Ye, Kim, & Kim, 2006; Sedki et al., 2018).
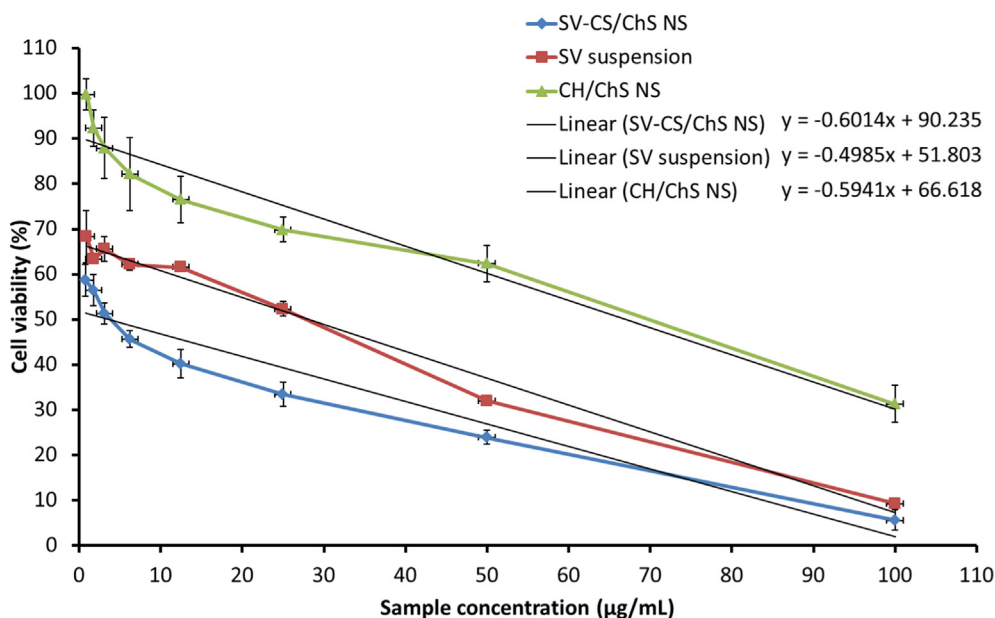

Fig. 6. Cell viability of HepG2 cells after incubation for 48 h at 37 °C with different SV suspensions and CS-ChSNPs and SV- CS-ChSNP concentrations.

Table 4
The IC $_{50}$ values and equations of equivalent regression line for different formulations curves.

Formulation	Equation	IC$_{50}$
SV suspension	y = -0.5941x + 66.618	28.15
CSChSNPs	y = -0.4985x + 51.803	63.85
SVCSChSNPs	y = -0.4697x + 87.737	3.67

3.10. In vitro cell uptake and detection of ASGPR-mediated endocytosis

In vitro intracellular uptake of the optimized SV-loaded CSChSNPs in the HepG2 cells was examined by fluorescent imag-

ing. The immunofluorescent images were prepared by staining the cell nuclei using Hoechst 33,258 (blue) and the RBITC-labeled CS/ChS nanoparticles (red) for the detection of intracellular localization. The localization of the SVCSChSNPs was detected by the red fluorescence of RBITC-labeled CS (emits fluorescence at k = 580 nm) after treating the HepG2 cells with the NPs for 4 h. The CS served a dual function as a part of the carrier system and as a dye carrier agent and hence an image marker.

In Fig. 8, the blank shows HepG2 cells without any treatment (no-treatment control, A, and B); the cells were flat and well-spread, indicating that their typical shape and surface morphology were retained during the 4 h of the experiment. No autofluorescence was detectable in the untreated control cells during this per-
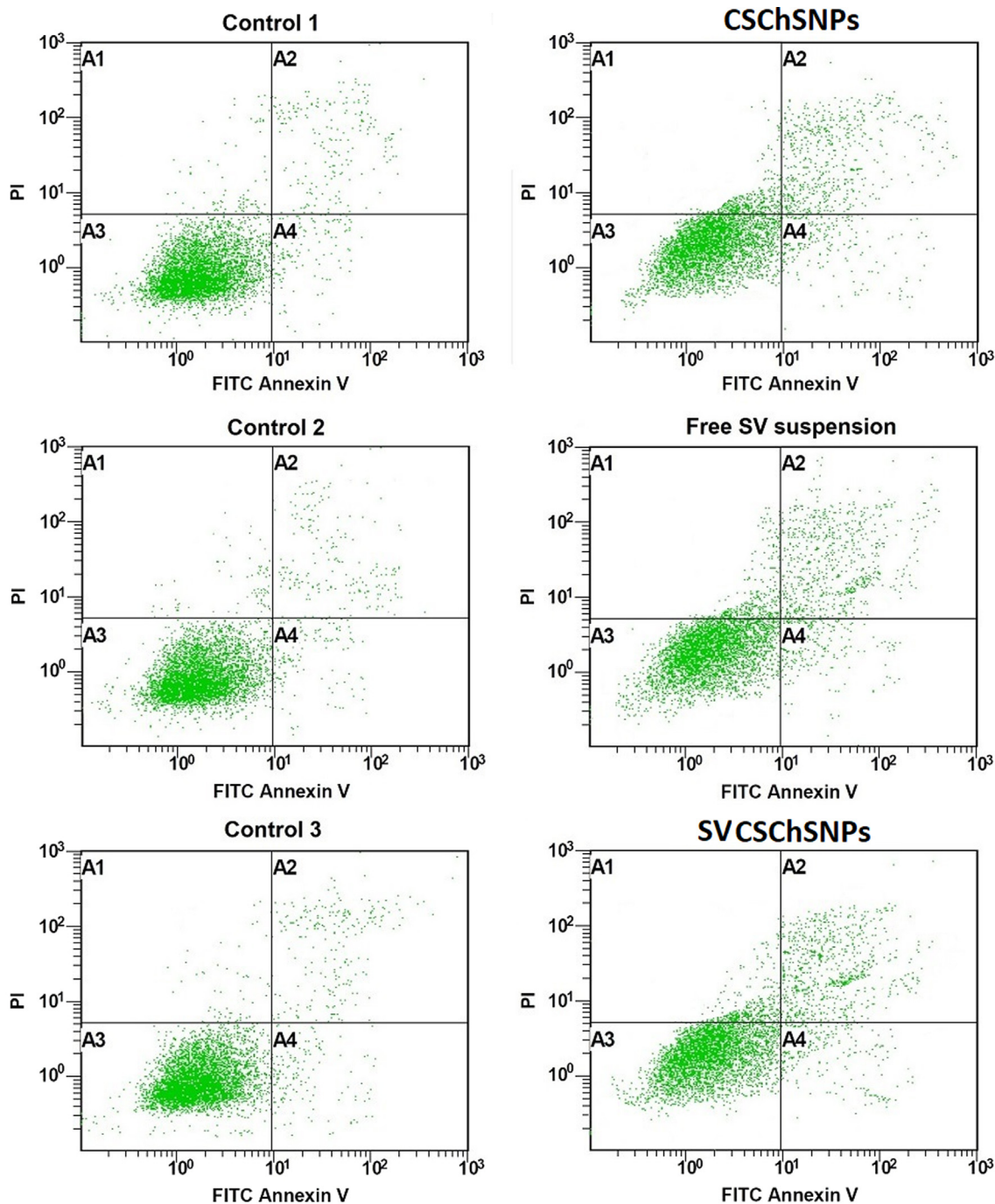

Fig. 7. Effect of CSChSNPs, free SV suspension, and SVCSChSNPs on the HepG2 cell apoptotic ratio. Cells early in the apoptosis (A4) were stained with the Annexin V FITC conjugate alone; live cells (A3) showed no staining by either the Propidium Iodide or Annexin V FITC conjugate.
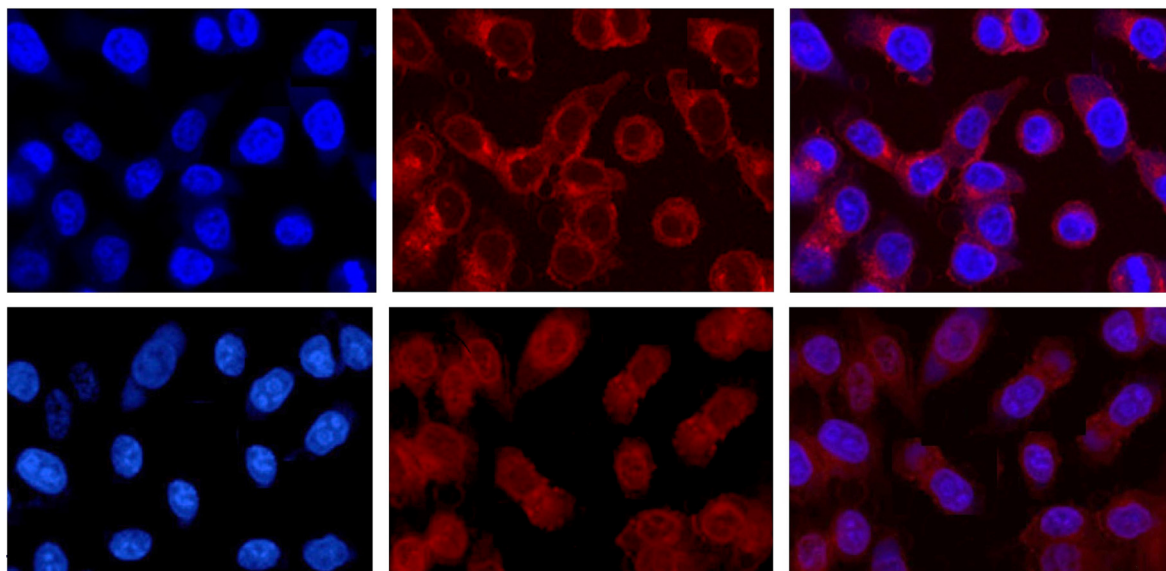
Fig. 8. Laser confocal microscope images for detection of intracellular uptake of the NPs by HepG2 cells following incubation at 37 °C for 4 h in the presence (A) and absence (B) of aqueous galactose. Blue channel–cell nucleus (Hoechst 33258®) A1 and B1; Red channel–SV-loaded RBITC-CS/ChS nanoparticles A2 and B2; Merged–superimposition of channels A3 and B3; (3) Mechanism suggested for NP cellular uptake showing ASGPRs and coupling with the GalNAc moiety.**Abbreviations:** SV, simvastatin; RBITC, rhodamine B isothiocyanate; CS/ChS nanoparticles, chitosan/chondroitin sulfate nanoparticles; ASGPRs, asialoglycoprotein receptors; GalNAc, N-acetylgalactosamine. (For interpretation of the references to color in this figure legend, the reader is referred to the web version of this article.)

iod. The images also showed that the NP-treated cells (A$_{1,2,3}$ and B$_{1,2,3}$) were well-spread and there was no distinct change in their morphology after 4 h incubation with nanoparticles as compared to the control cells. After 4 h uptake, in the case of B$_3$, a large amount of red fluorescence was detectable in the cytosol but not in the nucleus, indicating the internalization of the NPs. In addition, a small number of the NPs were internalized by cells preincubated with galactose (A$_3$). This could be attributed to the saturation of the ASGR with galactose, which acts as a competitor ligand for GalNAc, resulting in a reduction in the uptake of the NPs. The expected mechanism for cellular uptake using the ASGPRs is shown in Fig. 9.
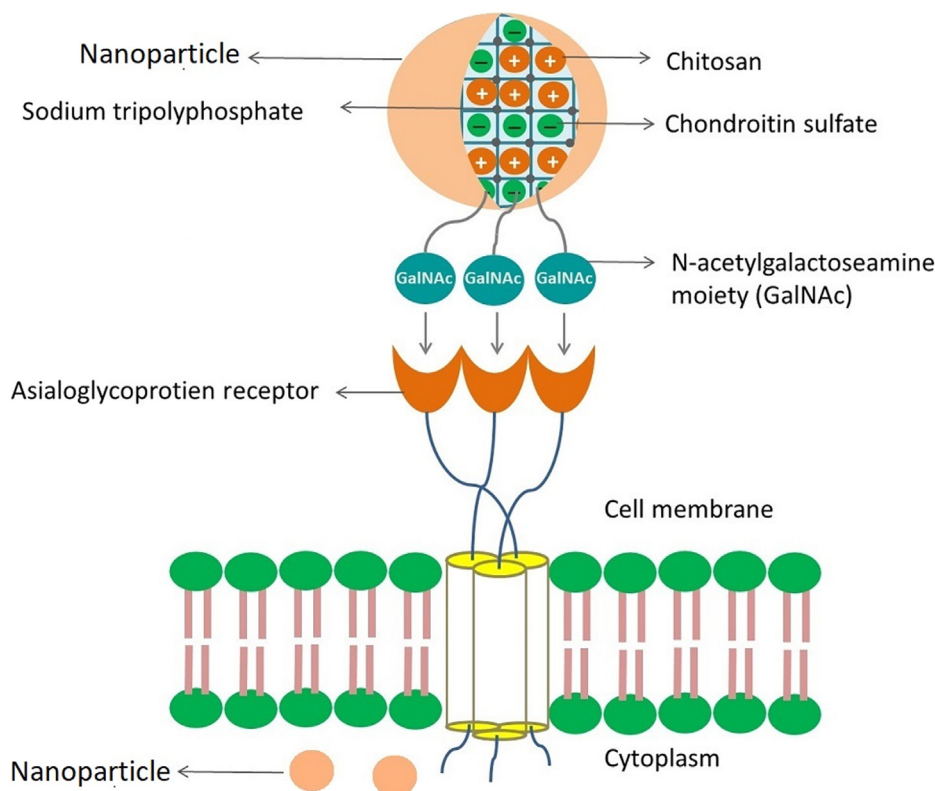
Fig. 9. Mechanism of SVCSChSNP cellular uptake showing ASGPR and coupling with the N-acetylgalactoseamine moiety in the nanoparticle.
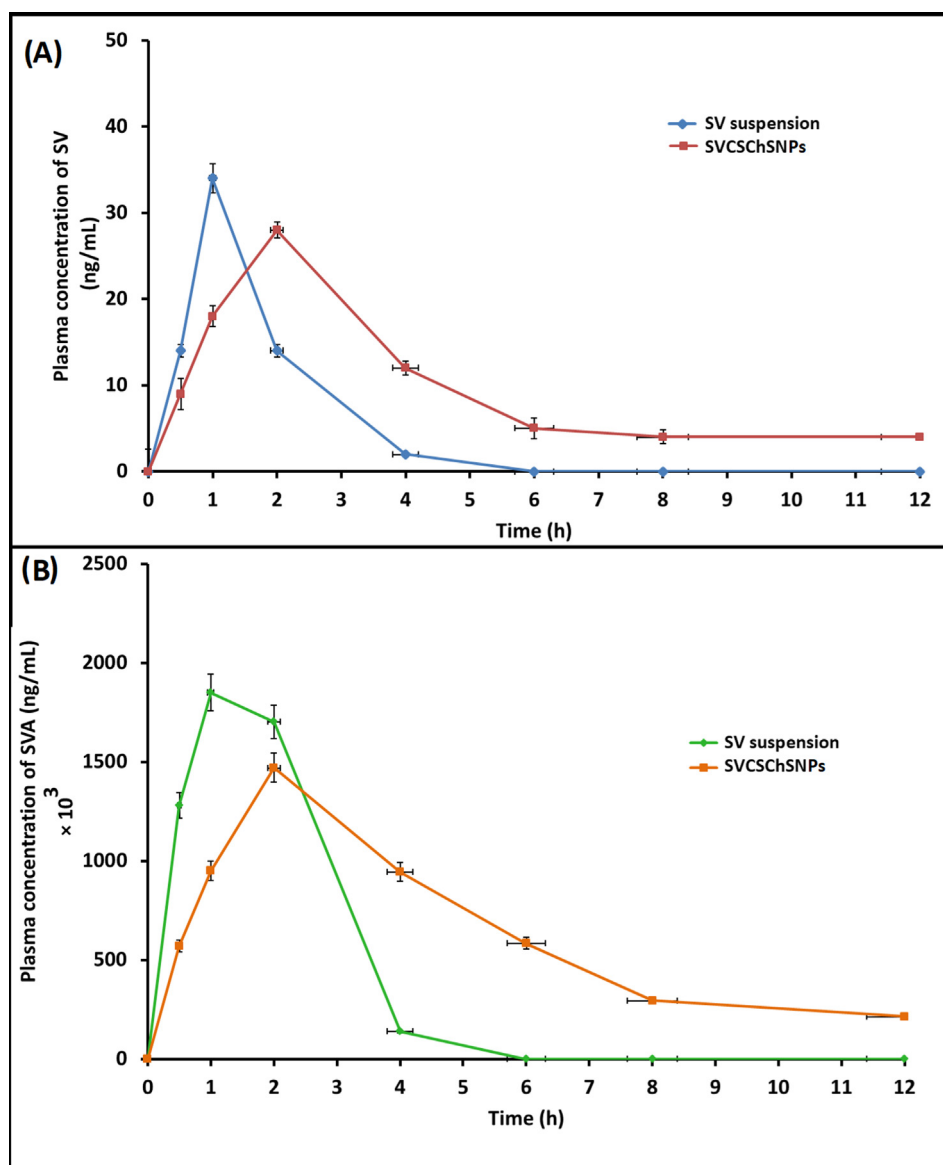
Fig. 10. The concentration–time profile of (A) SV, (B) SVA in Wister albino rat plasma after a single oral dose (20 mg/kg) of SV suspension, SV-CSNPs, and SV-CS/ChSNPs (n = 6).

Harisa and Faris reported that the size and charge of the nanocarriers plays a key role in their adhesion to and different interactions with the cell membrane. The nanocarriers of size<200 nm undergo receptor-mediated endocytosis, while particles with more than such size are engulfed by phagocytosis. Cationic NPs can directly bind to a cell's negatively charged cell membrane and induce cellular uptake (Harisa & Faris, 2019). In the current study, the prepared NPs were with a positive charge and may enter the cell by the caveolae-mediated pathway, which mainly contributes particles with diameters<80 nm because the caveolar endocytic vesicles are approximately 50–80 nm in diameter (Jiang et al., 2017). Further studies are required to detect the cellular uptake mechanism of the NPs and to estimate the number of NPs taken up by the cells during different periods.

3.11. In vivo pharmacokinetic study

The SV must be biotransformed into its pharmacologically active metabolite SVA before it provided the biological effect (Nirogi et al., 2007). Based on this, the *in vivo* pharmacokinetic

behavior for both SV and its metabolite SVA in Wistar rat plasma were assessed. The plasma concentration–time profiles of the SV and SVA after oral administration of a single dose of pure SV suspension of SVCSChSNPs to Wistar rats are shown in Fig. 10, and the corresponding pharmacokinetic parameters are presented in Table 5. The calculation of pharmacokinetic parameters followed non-compartmental model.

In terms of its pharmacokinetic profile, SV was rapidly absorbed from the SV suspension and the polymeric NPs, with maximum plasma concentrations observed within 1–2 h post-dose, followed by a rapid decrease in concentration below the limit of detection after 12 h. The C_{max} of the SV suspension was large compared to that of the NPs. At the same time, the T_{max} of the NPs was 2-fold that of the SV suspension. This variation occurred because the developed NPs released the SV slowly, resulting in an approximately 2-fold increase in the AUC_{0-12}. This is a significant enhancement compared to previous studies, where SV bioavailability was improved 1.9-fold when formulated as a complex (Kong et al., 2018). The current results are consistent with reports of 2-, 2.5-, and 3-fold improvement when formulated as silica-lipid

Table 5
Pharmacokinetic parameters of SV and SVA after oral administration of pure SV suspension and SVCSChSNPs to Wistar rats.

PK parameter	SV		SVA	
	SV suspension	SVCSChSNPs	SV suspension	SVCSChSNPs
T_{max} (h)	1 ± 0.1	2 ± 0.1	1 ± 0.1	2 ± 0.1
C_{max} (ng/mL)	34 ± 1.3	28 ± 1.6	1850 ± 155	1470 ± 152
$AUC_{0\rightarrow12}$ (ng.h /mL)	54.5 ± 1.2	114 ± 1.4	4720.5 ± 105	7566.5 ± 166
$T_{1/2}$ (h)	0.57 ± 0.1	3.63 ± 0.2	0.75 ± 0.5	3.4 ± 0.9
F_{REL} (%)	100	160.3	100	209.2
MRT (h)	1.42 ± 1	5.99 ± 0.4	1.67 ± 0.4	5.79 ± 0.4
Vz/F (mg)/(ng/mL)	0.07	0.016	0.001	0.002
Cl/F (mg)/(ng/mL)/h	0.07	0.03	0.001	0.0005

Each value represents the mean ± SD (n = 6).

hybrid (Meola et al., 2020) polymeric nanoparticles coated with caseinate (Ahmed et al., 2015) and dendrimers (Qi et al., 2015), respectively.

Table 4 shows that the $T_{1/2}$ of SV after oral administration as CSChSNPs was improved by up to 6.3- and 3.4-fold for SV and SVA, respectively, compared to the reference SV suspension. CSChSNPs increased the pharmacological half-life ($T_{1/2}$) of the SV owing to a reduction in the rate of transfer of the delivery system from the stomach to the intestine. This action improves drug absorption by increasing the time required for digestion and drug dissolution, thus prolonging the pharmacological efficacy (Meola et al., 2020). The results suggest that the aqueous solubility and hence intestinal absorption was significantly improved after the SV was incorporated in the CSChSNPs. The developed polymeric technology can extend drug exposure, improving the drug effect.

The CSChSNPs provided up to 2-fold improvement in SV AUC_{0-12} (bioavailability) compared to the pure SV suspension. The C_{max} of the drug suspension was greater than that of the NPs, despite the 4.5-fold enhancement in exposure owing to the extended drug $T_{1/2}$. As expected, T_{max} was delayed up to 2-fold for the NPs compared to the SV suspension owing to the time required for the release of the drug from the polymeric matrix. The obtained NPs enhanced SVA bioavailability 1.6-fold compared to the drug suspension. Importantly, the overall bioavailability enhancement provided by NPs was greater for SVA than for SV, which is desirable because SVA is responsible for therapeutic efficacy.

Additionally, in comparison to previous reports, superior SVA exposure was observed for the CSChSNPs. Zhang and team developed a SV/Soluplus solid dispersion and found a 1.7-fold enhancement in the bioavailability of SVA compared to a commercial SV solid dispersion tablet when administered to beagle dogs (Zhang et al., 2016). Meola and colleague developed SV silica-lipid hybrid microparticles and found a 1.2-fold improvement in the bioavailability of SVA compared to a reference SV suspension when administered to rats (Meola et al., 2020). Furthermore, a pharmacokinetic study in rats investigating SV lipid-based formulation demonstrated a 2-fold increase in SVA exposure compared to the SV suspension (Zhang et al., 2010a,b). This suggests that CSChSNPs provide additional benefits compared to previous studies, resulting in greater SVA exposure.

In the current study, CS was used because its cationic charge allows it to act as an anticancer manner and enhance the action of anticancer agents (Jiang et al., 2019). Moreover, CS is soluble in acidic pH values, as in the case of the tumor environment, which results from the increased glycolysis and proton-pump activity of cancer cells (Li & Xie, 2017; Sun et al., 2019). ChS was used to provide active targeting via ASGPRs overexpressed on the surface of hepatocytes, which are less common in non-liver cells and have a high affinity for ChS GalNAc moieties. Additionally, ChS increased the crosslinking rigidity of the CSNPs and hence slowed the fast release of the drug from the obtained NPs. The balance between

NP positive charges and negative charges forms virus-like surfaces, thereby increasing mucus penetration (Wu et al., 2018). In the current study, the NPs' ultrafine particle size and spherical and oval morphology patterns as well as their cationic charge allowed better penetration of cell membrane and intracellular localization (Harisa & Faris, 2019). Safwat et al. (2017) showed that properly formulated NPs enhance statins targeting to the carcinogenic cells and accordingly reduce drug quantity could be used.

4. Conclusion

In the present study, ultrafine (<100 nm) SVCSChSNPs were successfully prepared. The obtained NPs elicited the control release pattern of the SV. The ultrafine particle size and positive surface charge of the developed NPs enhanced the accumulation of SV in the intracellular compartments. ChS decoration of SVCSNPs enhanced the cytotoxicity of the SV against HepG2 cells owing to its enhanced cellular uptake. Furthermore, ChS decoration of SVCSNPs improved the oral bioavailability of the SV compared to SV suspension. Further studies are needed to address the use of SVCSChSNPs against hepatic cancer using an animal model for HCC.

Acknowledgment

References

Abdullah, T.A., Ibrahim, N.J., Warsi, M.H., 2016. Chondroitin Sulfate-chitosan Nanoparticles for Ocular Delivery of Bromfenac Sodium: Improved Permeation, Retention, and Penetration. Int. J. Pharm. Investig., p. 6.

Ahmed, O.A.A., Hosny, K.M., Al-Sawahli, M.M., Fahmy, U.A., 2015. Optimization of caseinate-coated simvastatin-zein nanoparticles: improved bioavailability and modified release characteristics. Drug Des. Devel. Ther. 9, 655–662. https://doi.org/10.2147/DDDT.S76194.

Alkhatib, M.H., Al-Merabi, S.S., 2014. In vitro assessment of the anticancer activity of simvastatin-loaded microemulsion in liver and colon cancer cells. J. Drug Deliv. Sci. Technol. 24, 373–379. https://doi.org/10.1016/S1773-2247(14)50076-7.

Barclay, T.G., Day, C.M., Petrovsky, N., Garg, S., 2019. Review of polysaccharide particle-based functional drug delivery. Carbohydr. Polym. 221, 94–112. https://doi.org/10.1016/j.carbpol.2019.05.067.

Bradbury, P., Traini, D., Ammit, A.J., Young, P.M., Ong, H.X., 2018. Repurposing of statins via inhalation to treat lung inflammatory conditions. Adv. Drug Deliv. Rev. 133, 93–106. https://doi.org/10.1016/j.addr.2018.06.005.

Bugnicourt, L., Ladavière, C., 2016. Interests of chitosan nanoparticles ionically cross-linked with tripolyphosphate for biomedical applications. Prog. Polym. Sci. 60, 1–17. https://doi.org/10.1016/j.progpolymsci.2016.06.002.

Calvo, P., Remuñán-López, C., Vila-Jato, J.L., Alonso, M.J., 1997. Novel hydrophilic chitosan-polyethylene oxide nanoparticles as protein carriers. J. Appl. Polym. Sci. 63, 125–132. https://doi.org/10.1002/(SICI)1097-4628(19970103)63:1<125::AID-APP13>3.0.CO;2-4.

Cho, S.-J., Kim, J.S., Kim, J.M., Lee, J.Y., Jung, H.C., Song, I.S., 2008. Simvastatin induces apoptosis in human colon cancer cells and in tumor xenografts, and attenuates

colitis-associated colon cancer in mice. Int. J. Cancer 123, 951–957. https://doi.org/10.1002/ijc.23593.

D'Souza, A.A., Devarajan, P.V., 2015. Asialoglycoprotein receptor mediated hepatocyte targeting — Strategies and applications. J. Control. Release 203, 126–139. https://doi.org/10.1016/j.jconrel.2015.02.022.

Fan, W., Yan, W., Xu, Z., Ni, H., 2012. Formation mechanism of monodisperse, low molecular weight chitosan nanoparticles by ionic gelation technique. Colloids Surfaces B Biointerfaces 90, 21–27. https://doi.org/10.1016/j.colsurfb.2011.09.042.

Faris, T., Harisa, G.I., Alanazi, F.K., Badran, M.M., Alotaibi, A.M., Alotaibi, H., Alqahtani, A.S., Samy, A.M., 2020. Cytotoxicity of chitosan ultrafine nanoshuttles on the MCF-7 cell line as a surrogate model for breast cancer. Curr. Drug Deliv. 17. https://doi.org/10.2174/1567201817666200719005440.

Fatehi Hassanabad, A., 2019. Current perspectives on statins as potential anti-cancer therapeutics: clinical outcomes and underlying molecular mechanisms. Transl. lung cancer Res. 8, 692–699 https://doi.org/10.21037/tlcr.2019.09.08.

Geboers, S., Stappaerts, J., Tack, J., Annaert, P., Augustijns, P., 2016. In vitro and in vivo investigation of the gastrointestinal behavior of simvastatin. Int. J. Pharm. 510, 296–303. https://doi.org/10.1016/j.ijpharm.2016.06.048.

George, A., Shah, P.A., Shrivastav, P.S., 2019. Natural biodegradable polymers based nano-formulations for drug delivery: A review. Int. J. Pharm. 561, 244–264. https://doi.org/10.1016/j.ijpharm.2019.03.011.

Harisa, G.I., Alomrani, A.H., Badran, M.M., 2017. Simvastatin-loaded nanostructured lipid carriers attenuate the atherogenic risk of erythrocytes in hyperlipidemic rats. Eur. J. Pharm. Sci. 96, 62–71. https://doi.org/10.1016/j.ejps.2016.09.004.

Harisa, G.I., Badran, M.M., AlQahtani, S.A., Alanazi, F.K., Attia, S.M., 2016. Pravastatin chitosan nanogels-loaded erythrocytes as a new delivery strategy for targeting liver cancer. Saudi Pharm. J. 24, 74–81. https://doi.org/10.1016/j.jsps.2015.03.024.

Harisa, G.I., Faris, T.M., 2019. Direct drug targeting into intracellular compartments: Issues, limitations, and future outlook. J Membr. Biol 252, 527–539. https://doi.org/10.1007/s00232-019-00082-5.

Hejjaji, E.M.A., Smith, A.M., Morris, G.A., 2018. Evaluation of the mucoadhesive properties of chitosan nanoparticles prepared using different chitosan to tripolyphosphate (CS:TPP) ratios. Int. J. Biol. Macromol. 120, 1610–1617. https://doi.org/10.1016/j.ijbiomac.2018.09.185.

Hu, C.-S., Tang, S.-L., Chiang, C.-H., Hosseinkhani, H., Hong, P.-D., Yeh, M.-K., 2014. Characterization and anti-tumor effects of chondroitin sulfate–chitosan nanoparticles delivery system. J. Nanoparticle Res. 16, 2672. https://doi.org/10.1007/s11051-014-2672-z.

Hu, C., Chiang, C., Hong, P., Yeh, M., 2012. Influence of charge on FITC-BSA-loaded chondroitin sulfate-chitosan nanoparticles upon cell uptake in human Caco-2 cell monolayers. Int. J. Nanomedicine 7, 4861–4872. https://doi.org/10.2147/IJN.S34770.

Iannelli, F., Lombardi, R., Milone, M.R., Pucci, B., De Rienzo, S., Budillon, A., Bruzzese, F., 2018. Targeting mevalonate pathway in cancer treatment: Repurposing of statins. Recent Pat. Anticancer. Drug Discov. 13, 184–200. https://doi.org/10.2174/1574892812666171129141211.

Jardim, K.V., Joanitti, G.A., Azevedo, R.B., Parize, A.L., 2015. Physico-chemical characterization and cytotoxicity evaluation of curcumin loaded in chitosan/chondroitin sulfate nanoparticles. Mater. Sci. Eng. C 56, 294–304. https://doi.org/10.1016/j.msec.2015.06.036.

Jardim, K.V., Siqueira, J.L.N., Báo, S.N., Sousa, M.H., Parize, A.L., 2020. The role of the lecithin addition in the properties and cytotoxic activity of chitosan and chondroitin sulfate nanoparticles containing curcumin. Carbohydr. Polym. 227,. https://doi.org/10.1016/j.carbpol.2019.115351 115351.

Jiang, L., Duan, H., Ji, X., Wang, T., Wang, Y., Qiu, J., 2018. Application of a simple desolvation method to increase the formation yield, physical stability and hydrophobic drug encapsulation capacity of chitosan-based nanoparticles. Int. J. Pharm. 545, 117–127. https://doi.org/10.1016/j.ijpharm.2018.03.044.

Jiang, L.Q., Wang, T.Y., Webster, T.J., Duan, H.-J., Qiu, J.Y., Zhao, Z.M., Yin, X.X., Zheng, C.L., 2017. Intracellular disposition of chitosan nanoparticles in macrophages: intracellular uptake, exocytosis, and intercellular transport. Int. J. Nanomedicine 12, 6383–6398. https://doi.org/10.2147/IJN.S142060.

Jiang, Y., Yu, X., Su, C., Zhao, L., Shi, Y., 2019. Chitosan nanoparticles induced the antitumor effect in hepatocellular carcinoma cells by regulating ROS-mediated mitochondrial damage and endoplasmic reticulum stress. Artif. Cells, Nanomedicine, Biotechnol. 47, 747–756. https://doi.org/10.1080/21691401.2019.1577876.

Karimi, B., Ashrafi, M., Shomali, T., Yektaseresht, A., 2019. Therapeutic effect of simvastatin on DMBA-induced breast cancer in mice. Fundam. Clin. Pharmacol. 33, 84–93. https://doi.org/10.1111/fcp.12397.

Kong, R., Zhu, X., Meteleva, E.S., Dushkin, A.V., Su, W., 2018. Physicochemical characteristics of the complexes of simvastatin and atorvastatin calcium with hydroxypropyl-β-cyclodextrin produced by mechanochemical activation. J. Drug Deliv. Sci. Technol. 46, 436–445. https://doi.org/10.1016/j.jddst.2018.05.018.

Kou, C.-H., Han, J., Han, X.-L., Zhuang, H.-J., Zhao, Z.-M., 2017. Preparation and characterization of the Adriamycin-loaded amphiphilic chitosan nanoparticles and their application in the treatment of liver cancer. Oncol. Lett. 14, 7833–7841. https://doi.org/10.3892/ol.2017.7210.

Li, R., Xie, Y., 2017. Nanodrug delivery systems for targeting the endogenous tumor microenvironment and simultaneously overcoming multidrug resistance properties. J. Control. Release 251, 49–67. https://doi.org/10.1016/j.jconrel.2017.02.020.

Li, Y.C., Park, M.J., Ye, S.-K., Kim, C.-W., Kim, Y.-N., 2006. Elevated levels of cholesterol-rich lipid rafts in cancer cells are correlated with apoptosis sensitivity induced by cholesterol-depleting agents. Am. J. Pathol. 168, 1107–1118. https://doi.org/10.2353/ajpath.2006.050959.

Matusewicz, L., Podkalicka, J., Sikorski, F.A., 2018. Immunoliposomes with simvastatin as a potential therapeutic in treatment of breast cancer cells overexpressing HER2—an in vitro study. Cancers (Basel). https://doi.org/10.3390/cancers10110418.

Meola, T.R., Schultz, H.B., Peressin, K.F., Prestidge, C.A., 2020. Enhancing the oral bioavailability of simvastatin with silica-lipid hybrid particles: The effect of supersaturation and silica geometry. Eur. J. Pharm. Sci. 150,. https://doi.org/10.1016/j.ejps.2020.105357 105357.

Muscella, A., Vetrugno, C., Migoni, D., Biagioni, F., Fanizzi, F.P., Fornai, F., De Pascali, S.A., Marsigliante, S., 2014. Antitumor activity of [Pt(O,O'-acac)(γ-acac)(DMS)] in mouse xenograft model of breast cancer. Cell Death Dis. 5, e1014–e1014. https://doi.org/10.1038/cddis.2013.554.

Nirogi, R., Mudigonda, K., Kandikere, V., 2007. Chromatography–mass spectrometry methods for the quantitation of statins in biological samples. J. Pharm. Biomed. Anal. 44, 379–387. https://doi.org/10.1016/j.jpba.2007.02.008.

Oesterle, A., Laufs, U., Liao, J.K., 2017. Pleiotropic effects of statins on the cardiovascular system. Circ. Res. 120, 229–243. https://doi.org/10.1161/CIRCRESAHA.116.308537.

Patil, P., Patil, V., Paradkar, A., 2007. Formulation of a self-emulsifying system for oral delivery of simvastatin: in vitro and in vivo evaluation. Acta Pharm. 57, 111–122. https://doi.org/10.2478/v10007-007-0009-5.

Pranatharthiharan, S., Patel, M.D., Malshe, V.C., Pujari, V., Gorakshakar, A., Madkaikar, M., Ghosh, K., Devarajan, P.V., 2017. Asialoglycoprotein receptor targeted delivery of doxorubicin nanoparticles for hepatocellular carcinoma. Drug Deliv. 24, 20–29. https://doi.org/10.1080/10717544.2016.1225856.

Qi, R., Zhang, H., Xu, L., Shen, W., Chen, C., Wang, C., Cao, Y., Wang, Y., van Dongen, M.A., He, B., Wang, S., Liu, G., Banaszak Holl, M.M., Zhang, Q., 2015. G5 PAMAM dendrimer versus liposome: A comparison study on the in vitro transepithelial transport and in vivo oral absorption of simvastatin. Nanomedicine Nanotechnology. Biol. Med. 11, 1141–1151. https://doi.org/10.1016/j.nano.2015.02.011.

Relja, B., Meder, F., Wang, M., Blaheta, R., Henrich, D., Marzi, I., Lehnert, M., 2011. Simvastatin modulates the adhesion and growth of hepatocellular carcinoma cells via decrease of integrin expression and ROCK. Int. J. Oncol. 38, 879–885. https://doi.org/10.3892/ijo.2010.892.

Relja, B., Meder, F., Wilhelm, K., Henrich, D., Marzi, I., Lehnert, M., 2010. Simvastatin inhibits cell growth and induces apoptosis and G0/G1 cell cycle arrest in hepatic cancer cells. Int. J. Mol. Med. 26, 735–741. https://doi.org/10.3892/ijmm_00000520.

Rezazadeh, M., Parandeh, M., Akbari, V., Ebrahimi, Z., Taheri, A., 2019. Incorporation of rosuvastatin-loaded chitosan/ chondroitin sulfate nanoparticles into a thermosensitive hydrogel for bone tissue engineering: preparation, characterization, and cellular behavior. Pharm. Dev. Technol. 24, 357–367. https://doi.org/10.1080/10837450.2018.1484765.

Ribeiro, T.G., Chávez-Fumagalli, M.A., Valadares, D.G., França, J.R., Rodrigues, L.B., Duarte, M.C., Lage, P.S., Andrade, P.H.R., Lage, D.P., Arruda, L.V., Abánades, D.R., Costa, L.E., Martins, V.T., Tavares, C.A.P., Castilho, R.O., Coelho, E.A.F., Faraco, A.A. G., 2014. Novel targeting using nanoparticles: an approach to the development of an effective anti-leishmanial drug-delivery system. Int. J. Nanomedicine 9, 877–890. https://doi.org/10.2147/IJN.S55678.

Rizvi, S.Z.H., Shah, F.A., Khan, N., Muhammad, I., Ali, K.H., Ansari, M.M., Din, F. ud, Qureshi, O.S., Kim, K.-W., Choe, Y.-H., Kim, J.-K., Zeb, A., 2019. Simvastatin-loaded solid lipid nanoparticles for enhanced anti-hyperlipidemic activity in hyperlipidemia animal model. Int. J. Pharm. 560, 136–143. https://doi.org/10.1016/j.ijpharm.2019.02.002.

Safwat, S., Ishak, R.A., Hathout, R.M., Mortada, N.D., 2017. Statins anticancer targeted delivery systems: re-purposing an old molecule. J. Pharm. Pharmacol. 69, 613–624. https://doi.org/10.1111/jphp.12707.

Sedki, M., Khalil, I.A., El-Sherbiny, I.M., 2018. Hybrid nanocarrier system for guiding and augmenting simvastatin cytotoxic activity against prostate cancer. Artif. Cells, Nanomedicine, Biotechnol. 46, S641–S650. https://doi.org/10.1080/21691401.2018.1505743.

Sharma, S., Swetha, K.L., Roy, A., 2019. Chitosan-Chondroitin sulfate based polyelectrolyte complex for effective management of chronic wounds. Int. J. Biol. Macromol. 132, 97–108. https://doi.org/10.1016/j.ijbiomac.2019.03.186.

Silva, T.D., Oliveira, M.A., de Oliveira, R.B., Vianna-Soares, C.D., 2012. Development and Validation of a Simple and Fast HPLC Method for Determination of Lovastatin, Pravastatin and Simvastatin. J. Chromatogr. Sci. 50, 831–838. https://doi.org/10.1093/chromsci/bms079.

Soe, Z.C., Poudel, B.K., Nguyen, H.T., Thapa, R.K., Ou, W., Gautam, M., Poudel, K., Jin, S.G., Jeong, J.-H., Ku, S.K., Choi, H.-G., Yong, C.S., Kim, J.O., 2019. Folate-targeted nanostructured chitosan/chondroitin sulfate complex carriers for enhanced delivery of bortezomib to colorectal cancer cells. Asian J. Pharm. Sci. 14, 40–51. https://doi.org/10.1016/j.ajps.2018.09.004.

Sun, Y., Ma, W., Yang, Y., He, M., Li, A., Bai, L., Yu, B., Yu, Z., 2019. Cancer nanotechnology: Enhancing tumor cell response to chemotherapy for hepatocellular carcinoma therapy. Asian J. Pharm. Sci. https://doi.org/10.1016/j.ajps.2019.04.005.

Turato, C., Balasso, A., Carloni, V., Tiribelli, C., Mastrotto, F., Mazzocca, A., Pontisso, P., 2017. New molecular targets for functionalized nanosized drug delivery systems in personalized therapy for hepatocellular carcinoma. J. Control. Release 268, 184–197. https://doi.org/10.1016/j.jconrel.2017.10.027.

Umerska, A., Corrigan, O.I., Tajber, L., 2017. Design of chondroitin sulfate-based polyelectrolyte nanoplexes: Formation of nanocarriers with chitosan and a case study of salmon calcitonin. Carbohydr. Polym. 156, 276–284. https://doi.org/10.1016/j.carbpol.2016.09.035.

Wang, S.-T., Ho, H.J., Lin, J.-T., Shieh, J.-J., Wu, C.-Y., 2017. Simvastatin-induced cell cycle arrest through inhibition of STAT3/SKP2 axis and activation of AMPK to promote p27 and p21 accumulation in hepatocellular carcinoma cells. Cell Death Dis. 8, e2626–e2626. https://doi.org/10.1038/cddis.2016.472.

Wang, X., Wu, F., Li, G., Zhang, N., Song, X., Zheng, Y., Gong, C., Han, B., He, G., 2018. Lipid-modified cell-penetrating peptide-based self-assembly micelles for co-delivery of narciclasine and siULK1 in hepatocellular carcinoma therapy. Acta Biomater. 74, 414–429. https://doi.org/10.1016/j.actbio.2018.05.030.

Wang, Y., Wang, S., Song, R., Cai, J., Xu, J., Tang, X., Li, N., 2019. Ginger polysaccharides induced cell cycle arrest and apoptosis in human hepatocellular carcinoma HepG2 cells. Int. J. Biol. Macromol. 123, 81–90. https://doi.org/10.1016/j.ijbiomac.2018.10.169.

World health organization, 2018. Latest global cancer data: Cancer burden rises to 18.1 million new cases and 9.6 million cancer deaths in 2018. Geneva..

Wu, L., Shan, W., Zhang, Z., Huang, Y., 2018. Engineering nanomaterials to overcome the mucosal barrier by modulating surface properties. Adv. Drug Deliv. Rev. 124, 150–163. https://doi.org/10.1016/j.addr.2017.10.001.

Yuan, N.-Y., Tsai, R.-Y., Ho, M.-H., Wang, D.-M., Lai, J.-Y., Hsieh, H.-J., 2008. Fabrication and characterization of chondroitin sulfate-modified chitosan membranes for biomedical applications. Desalination 234, 166–174. https://doi.org/10.1016/j.desal.2007.09.083.

Zhang, Y., Huo, M., Zhou, J., Xie, S., 2010a. PKSolver: An add-in program for pharmacokinetic and pharmacodynamic data analysis in Microsoft Excel. Comput. Methods Programs Biomed. 99, 306–314. https://doi.org/10.1016/j.cmpb.2010.01.007.

Zhang, Y., Liu, Y., Luo, Y., Yao, Q., Zhong, Y., Tian, B., Tang, X., 2016. Extruded Soluplus/SIM as an oral delivery system: characterization, interactions, in vitro and in vivo evaluations. Drug Deliv. 23, 1902–1911. https://doi.org/10717544.2014.960982.

Zhang, Z., Bu, H., Gao, Z., Huang, Y., Gao, F., Li, Y., 2010b. The characteristics and mechanism of simvastatin loaded lipid nanoparticles to increase oral bioavailability in rats. Int. J. Pharm. 394, 147–153. https://doi.org/10.1016/j.ijpharm.2010.04.039.

Zhao, Z., Ukidve, A., Krishnan, V., Mitragotri, S., 2019. Effect of physicochemical and surface properties on in vivo fate of drug nanocarriers. Adv. Drug Deliv. Rev. https://doi.org/10.1016/j.addr.2019.01.002.